Leaflet specific phospholipid imaging using genetically encoded proximity sensors

William M. Moore[1], Roberto J. Brea[1§], Caroline Knittel[1], Ellen Wrightsman[1], Brandon Hui[1], Jinchao Lou[2], Christelle F. Ancajas[2], Michael D. Best[2], Neal K. Devaraj[1], and Itay Budin[1*]

[1] Department of Chemistry and Biochemistry, University of California San Diego, 9500 Gilman Drive, La Jolla, California 92093

[2] Department of Chemistry, The University of Tennessee, Knoxville, Tennessee 37996

§ Current address: Centro Interdisciplinar de Química e Bioloxía (CICA), Universidade da Coruña, Rúa As Carballeiras, 15701 A Coruña, Spain

* To whom correspondence should be addressed: ibudin@ucsd.edu

Abstract

The lipid composition of cells varies widely across organelles and between individual membrane leaflets. Transport proteins acting within and between membranes are thought to generate this heterogeneity, but measuring their functions has been hampered by limited tools for imaging lipid composition at relevant spatial resolutions. Here we present fluorogen-activating coincidence sensing (FACES), a chemogenetic tool capable of quantitatively imaging subcellular lipid pools and reporting their transbilayer orientation in living cells. FACES combines bioorthogonal chemistry with genetically encoded fluorogen-activating proteins (FAPs) for reversible proximity sensing of conjugated molecules. We first apply this approach to identify roles for lipid transfer proteins (LTP) that traffic phosphatidylcholine pools between the ER and mitochondria. We then show that transmembrane domain-containing FAPs can be used to reveal the membrane asymmetry of multiple lipid classes that is generated at the trans-Golgi network (TGN). Using FACES, we show how the asymmetry of a phosphatidylserine analogue at the TGN is supported by the activity of both cytosolic LTPs and transmembrane flippases. Lastly, we demonstrate that FACES is a generalizable tool for subcellular detection of other molecule classes by measuring changes in mitochondrial *N*-acetylhexosamine levels. These results introduce the application of fluorogenic tags for spatially-defined molecular imaging.

Introduction

Lipid composition determines the biophysical properties of cell membranes and varies across every scale of biological organization[1–3]. In cells, membrane heterogeneity between organelles is generated at contact sites, hot zones of lipid transport where opposing organelles are in close proximity; often only tens of nm apart[4,5]. While many lipid transfer proteins (LTP) acting at these sites have now been biochemically characterized[6,7], measuring their in vivo functions remains challenging. Within organelles, it has long been recognized that each bilayer leaflet – separated by less than 4 nm – could feature a unique lipidome, which is reflected in the biophysical properties of each leaflet and the topology of protein transmembrane domains[8]. Detailed lipidomic investigation of membrane asymmetry has only been carried out in the PM of erythrocytes, whose lack of intracellular compartments allow for calculation of lipid accessibility to externally added phospholipases[3,9]. While asymmetry is an emerging concept in membrane biology, the transbilayer distribution of phospholipids in intracellular membranes and its molecular drivers are still poorly understood.

Investigating membrane chemical heterogeneity remains a challenge due to the paucity of tools for imaging lipids in live cells at spatial resolutions needed to investigate lipid transport or asymmetry. Bioorthogonal ‘click’ chemistry has emerged as one tool for fluorescence labeling of specific lipid classes – including phosphatidylcholine (PC)[10], phosphatidylserine (PS)[11], phosphatidylinositol (PI)[12], phosphatidic acid[13], and glycosphingolipids[14] – that can be metabolically tagged with azide-bearing head group components (Fig. 1a). Azido (N_3) lipids are commonly conjugated to fluorophores using strain-promoted azide-alkyne cycloaddition (SPAAC) reactions, unveiling their cellular distribution once unreactive dyes are washed out. While powerful, this approach indiscriminately labels all lipids in the cell, and is thus limited by the resolution constraints of light microscopy; it cannot discriminate between lipid pools in

organelles at close proximity or in individual leaflets of the same membrane, for example. To overcome some of these limitations, organelle-targeted fluorophores have been applied to image subcellular lipid pools[15], but their specificity is limited to just a few chemical environments in the cell.

We hypothesized that challenges for lipid imaging could be overcome using protein-based lipid sensors, whose localization is precisely controlled through signal sequences or fusion to transmembrane domains. Previously, natural lipid binding proteins derived from microbial toxins, such as perfringolysin O[16] (cholesterol) or equinatoxin II[17] (sphingomyelin, SM) have been expressed as fusions with fluorescent proteins (FP), to detect membranes enriched in the target lipids. In these modalities, lipids are only qualitatively detected by colocalization of a probe to a membrane, which limits their application to large, well-separated compartments. We asked whether fluorogenic systems could provide a more generalizable strategy. Fluorogen-activating proteins (FAPs) can be expressed as fusion constructs with other proteins or targeting sequences, similar to FPs, but are not themselves fluorescent[18]. Instead, they interact with fluorogens, small cell-permeable molecules that act as fluorophores only upon specific binding to a FAP (Fig. 1b). Depending on the FAP used, fluorogen binding can be irreversible or reversible; the former provides brighter fluorescence for conventional imaging, while the latter generates stochastic blinking that can be harnessed for super-resolution imaging[19]. Recently, FAP domains have been applied towards detecting and controlling protein proximity in living cells through reversible dimerization[20], demonstrating that this technology can be harnessed in new applications.

We sought to harness the unique properties of fluorogens through Fluorogen-Activating Coincidence Sensing (FACES), which uses the FAP protein for proximity-dependent reporting of fluorogen conjugated bioorthogonal metabolites, including lipids. To accomplish this, we

89 synthesized fluorogenic dyes based on malachite green (MG) that are functionalized with a
90 dibenzocyclooctyne (DBCO) group for SPAAC reactions with azido-labeled metabolites in living
91 cells (Fig. 1c). In the FACES workflow (Fig. 1d), cells first express a FAP protein fused to an FP,
92 like GFP, that is targeted to an organelle or site of interest. Cells are then incubated with
93 azido-labeled metabolites for metabolic incorporation. Immediately before imaging, incorporated
94 metabolites are labeled with fluorogen-DBCO, which remains non-fluorescent unless it is
95 proximal to the expressed FAP. Excess dye is removed from cells by washing with culture
96 medium, leveraging the reversibility of FAP binding to minimize detection of unreacted
97 fluorogens. Subsequent ratiometric fluorescence imaging allows organelle-specific detection of
98 fluorogen conjugates by coincidence sensing with the FAP receptor. The abundance of the
99 target molecule is then quantified at the locale of interest by measuring the ratio of
100 FAP-fluorogen fluorescence, which represents the bound state of the FAP and is at red shifted
101 wavelengths for MG, to that of a green of blue reporter FP, which is used to normalize the rate of
102 detection to the concentration of the FAP receptor.
103
104 Here we apply the FACES strategy to investigate the transport of N_3-phospholipids in cells.
105 Ratiometric imaging with FACES enabled changes in N_3-lipid content of membranes to be
106 quantified, which we first use to characterize the role of ER-mitochondrial PC transporters. We
107 then show that transmembrane-anchored FAPs can probe leaflet-specific membrane
108 composition, identifying features and drivers of asymmetry generated during vesicle formation at
109 the trans-Golgi network (TGN). Lastly, we demonstrate that FACES is a broadly applicable tool
110 compatible with non-lipid metabolites by measuring fluctuations in mitochondrial
111 *N*-acetylhexosamine (HexNAz) levels.
112
113

Results

Development and validation of FACES

We synthesized derivatives of MG with a linker and DBCO group, compatible with copper-free SPAAC reactions, including compound **1a** (Fig. 1c; Supplementary Fig. 1). MG non-covalently binds to single-chain antibody scFvs FAP and the complex emits far-red fluorescence. We tested the compatibility and fluorogenic properties of **1a** with FACES using the FAP clone dH6.2, a lower affinity scFvs variant developed for reversible equilibrium binding to MG[21]. In all experiments, we fused dH6.2 – from here on simply referred to as FAP – to GFP for ratiometric imaging. A secretion signal and KDEL retention sequence were first used to target FAP-GFP to the endoplasmic reticulum (ER) as the major site of PC synthesis[22], while GFP-KDEL, an identical construct but lacking the FAP domain, was used as a control. HeLa cells transfected with either FAP-GFP-KDEL or GFP-KDEL were grown for 24h in the presence or absence of 50 μM N_3-Cho. At concentrations up to 100 μM, N_3-Cho was incorporated into PC at a frequency up to 0.1 mol %, but cells showed no detectable N_3-Cho incorporation into SM (Supplementary Fig. 2). Prior to staining, cells were washed and grown in normal growth media for 30 min to allow for the metabolic consumption of any remaining N_3-Cho. Cells were then transferred into FBS-free growth media containing 500 nM **1a** and imaged while in the staining solution (Supplementary Fig. 3a). Images were collected using identical acquisition and processing settings.

Results from pre-washed cells demonstrated that **1a** was cell permeable and generated strong far-red fluorescence in cells expressing FAP-GFP-KDEL (Supplementary Fig. 3a). No far-red fluorescence was detected in cells expressing GFP-KDEL, indicating that **1a** was not activated directly by conjugation to N_3-PC. Next we tested the reversibility of the FAP-fluorogen complex

140 by washing cells with growth medium and re-imaging. Three washes were sufficient to
141 dissociate free **1a** from FAP-GFP-KDEL cells in the absence of N_3-Cho, resulting in the loss of
142 far-red fluorescence. In contrast, far-red fluorescence was retained in FAP-GFP-KDEL cells that
143 were fed 50 μM N_3-Cho, which implicated the SPAAC reaction product **1a**-PC as the source of
144 FAP-dependent fluorescence (Supplementary Fig. 3b). Similar experiments with a higher affinity
145 FAP variant retained far-red fluorescence after washing in the absence of N_3-Cho labeling
146 (Supplementary Fig. 4), indicating that the reversible binding to the MG product is essential for
147 substrate-specific detection.
148
149 We further quantified these results in repeated experiments using confocal laser scanning
150 microscopy (CFLSM) to assess linear fluorescent detection. Cells transfected with
151 FAP-GFP-KDEL were fed 10, 30, or 50 μM N_3-Cho for 24h, while FAP-GFP-KDEL (no N_3-Cho)
152 and GFP-KDEL (+ 50 μM N_3-Cho) conditions were used as controls. All cells were stained with
153 500 nM **1a** and were washed as previously described; the **1a**-PC reaction product was
154 confirmed by LC-MS/MS (Supplementary Fig. 5). Fluorescence intensity profiles revealed that
155 far-red fluorescence from **1a** was tightly correlated with GFP fluorescence in FAP-GFP-KDEL
156 cells fed 50 μM N_3-Cho (Fig. 1e). In contrast, cells from either control condition, lacking the FAP
157 or N_3-Cho component, had low levels of far-red fluorescence that did not correlate with GFP
158 localization. The average fluorescence intensity from 10 cells, using 10 individual ER segments
159 per cell, was calculated as a ratiometric average relative to GFP (Fig. 1f). There was no
160 intensity difference between either control condition, while signal from FAP-GFP-KDEL cells fed
161 50 μM N_3-Cho was 10-fold higher. Additionally, **1a**-PC fluorescence was linearly dependent on
162 N_3-Cho concentration in the medium (Fig. 1g). We further tested whether the FACES signal was
163 a consequence of free N_3-Cho, as opposed to membrane incorporated N_3-PC, by using
164 compound D609 to pharmacologically perturb PC metabolism[23–25]. Cells treated with 50 μM
165 D609 during the 24h N_3-Cho incorporation period decreased FACES fluorescence by 50%

166 relative to untreated cells, despite being exposed to identical concentrations of N_3-Cho and **1a**
167 (Fig. 1h). Together, these results indicate that FACES is capable of linear fluorescent
168 quantification of N_3-PC, via its SPAAC reaction product **1a**-PC, in the ER of living cells.
169
170 Lipid transporters contributing to PC trafficking between ER and mitochondria
171
172 PC is the most abundant lipid in mammalian cells and is a component of all organelle
173 membranes, which make disentangling its subcellular transport mechanisms challenging. To
174 demonstrate the utility of the FACES method in illuminating organelle selective lipid pools, we
175 used the OTC mitochondrial targeting sequence (MTS) to direct FAP-GFP to the mitochondrial
176 matrix. Cells expressing MTS-FAP-GFP and the ER marker Sec61b-mCherry showed that
177 **1a**-PC detected in mitochondria did not overlap with the ER (Fig. 2a). Likewise, cells
178 co-expressing FAP-GFP-KDEL and Mito-BFP show that **1a**-PC detected in the ER did not
179 overlap with mitochondria (Fig. 2b).
180
181 When quantifying the performance of FACES in the mitochondrial matrix using CFLSM, we
182 found that switching the C6 alkane linker in **1a** to a polyethylene glycol (PEG)-2 linker
183 (compound **1b**) was beneficial for dissociating unreacted dye from this compartment. Similar to
184 the ER-targeted protein, MTS-FAP-GFP detection of **1b**-PC generated fluorescence that linearly
185 correlated with N_3-Cho concentration (Supplementary Fig. 6a-c). Using super-resolution
186 lattice-structured illumination microscopy (lattice SIM^2), we further tested whether the matrix
187 soluble FAP could resolve structural features of the IMM. When imaged by lattice SIM^2, FACES
188 signal from **1b**-PC occurred in a banding pattern distinct from the general distribution of the
189 probe (GFP signal) in the mitochondrial matrix (Supplementary Fig. 6d). Fluorescence intensity
190 profiles drawn across individual mitochondria show undulating peaks, with alternating maxima
191 between **1b**-PC and GFP. We interpreted this localization pattern as reflecting regions of high

192 cristae density in the IMM that contrast with void areas of the matrix[26], as previously observed
193 for mitochondrial PC[15].
194
195 Utilizing the ability to quantify PC in mitochondria and ER, we tested how defects in lipid
196 transport differentially affect these pools. For this, we generated stable cell lines expressing
197 either FAP-GFP-KDEL (ER) or MTS-FAP-GFP (mitochondria) for further experiments. PC is
198 synthesized in the ER and is transported to mitochondria by lipid transport proteins (LTPs)[22,27].
199 We used siRNA to silence two LTPs: VPS13a, a bridge-type LTP that interacts with VAPB at
200 ER-mitochondria contact sites and transports bulk phospholipids[28], and STARD7, a small
201 shuttle-type LTP that localizes to the mitochondrial intermembrane space and is thought to
202 transport PC between outer and inner membranes[29–31] (Fig. 2c). Silencing resulted in a >50%
203 reduction in both VPS13a and STARD7 protein content in each experiment (Supplementary Fig.
204 7). VPS13a and STARD7 siRNAs reduced **1b**-PC fluorescence in mitochondria, by 50% and
205 35% respectively, relative to negative control (NC) siRNA treated cells (Fig. 2d, e). However,
206 only knockdown of VPS13a increased **1a**-PC fluorescence in the ER (Fig. 2f, g), consistent with
207 its proposed role as an ER to mitochondrial PC LTP and that of STARD7 as an
208 intra-mitochondrial LTP. The magnitude of **1b**-PC reduction in mitochondria was larger upon
209 knockdown of VPS13a than for that of STARD7, suggesting that the former is a dominant
210 mechanism for bulk PC transport to mitochondria.
211
212 <u>Transbilayer asymmetry of multiple phospholipids generated at the trans-Golgi network</u>
213
214 There currently exist few, if any, tools capable of measuring membrane asymmetry in living
215 cells. We asked if the spatial specificity of FACES could provide this capacity when FAPs are
216 fused to the transmembrane domain for leaflet-specific fluorogen detection. A potential site of
217 asymmetry generation in the secretory pathway is at the TGN, where vesicles bud off from the

218 Golgi for trafficking of proteins and lipids to the highly asymmetric PM. We explored asymmetric
219 lipid detection in the TGN by reciprocal tagging of the transmembrane protein TGN38, at N- and
220 C-termini, to selectively orient FAPs toward either the exoplasmic or cytoplasmic facing leaflets
221 of the TGN (Fig. 3a). TGN38 cycles to and from the PM via secretory vesicles and recycling
222 endosomes[32], thereby labeling a split population of trans-Golgi cisternae and trans-Golgi
223 network vesiculated compartments[33].
224
225 Imaging of stable cells expressing GFP-TGN38-FAP, oriented towards the cytoplasmic leaflet,
226 and FAP-TGN38-GFP, oriented towards the luminal leaflet, detected fluorogen fluorescence of
227 **1a**-PC on both leaflets in cisternae and vesicles (Fig. 3b). However, the abundance shifted
228 between these compartments, comparatively enriching in the cytoplasmic leaflet in TGN
229 vesicles (Fig. 3c, Supplementary Fig. 8a). Lateral segregation between luminal **1a**-PC enriched
230 and depleted regions could be observed at sites of vesicular budding from the TGN
231 (Supplementary Fig. 9). These results are consistent with previous measurements of PC in
232 freeze-fractured yeast cells, also showing a cytoplasmic leaflet enrichment arising in the Golgi[34].
233
234 We next asked if FACES could measure the asymmetry of non-choline lipids at the TGN.
235 Recently, metabolic incorporation of azide containing L-serine[11] (C-L-Ser-N_3) and *myo*-inositol[12]
236 (Ino-N_3) have been shown to label phosphatidylserine (PS) and phosphatidylinositol (PI),
237 respectively. Both these lipid classes are synthesized in the ER and have been proposed to be
238 trafficked to the cytoplasmic leaflet of the trans-Golgi and TGN through lipid transfer proteins[35,36].
239 When analyzed with FACES, we observed **1a**-PI in Golgi cisternae that was evenly distributed
240 between luminal and cytoplasmic leaflets (Fig. 3b, Fig. 3c, Supplementary Fig. 8b). In TGN
241 vesicles, the distribution of **1a**-PI shifted to the cytoplasmic leaflet, similar to that for PC. For
242 **1a**-PS, using C-L-Ser-N_3, there was an absence of signal on both leaflets of Golgi cisternae and
243 a high, exclusively cytoplasmic abundance on TGN vesicles (Fig. 3b, Fig. 3c, Supplementary

Fig. 8c). This is consistent with previous observations that the PS-binding C2 domain of lactadherin, when expressed in the cytoplasm, robustly labels TGN vesicles, but not Golgi cisternae[37]. As a control for these cytosolic leaflet-enriched phospholipids, we imaged the distribution of surface glycans in cells fed with peracetylated *N*-azidoacetylmannosamine (Ac_4ManNAz)[38], which is metabolized into sialic acid (Sia) within the cell. We measured an exclusively luminal distribution of **1a**-Sia (Fig. 3b, Fig. 3c, Supplementary Fig. 8d) in both cisternae and vesicles, consistent with the synthesis of protein and lipid surface glycans in the Golgi lumen[39]. Lastly, co-staining cells expressing mCer3-TGN38-FAP (Blue FP variant) with equimolar amounts **1a** and BODIPY-DBCO, a conventional fluorophore, demonstrated that FACES can spectrally separate organelle-specific lipid pools that overlap with total cellular phospholipid distributions (Supplementary Fig. 10)

Previous analyses of TGN vesicles[40] and the PM[41] suggest that loss of luminal phospholipids could be substituted with SM, which is predominantly synthesized in the TGN and packaged in secretory vesicles. Consistent with this model, we observed that the SM probe SMeqt-GFP co-localized with vesicles enriched with cytoplasmic leaflet **1a**-PC (Fig. 3d). These vesicles shuttled rapidly between the Golgi and PM (Supplementary Movie 1). Similar results were obtained for vesicles labeled with the secretory cargo mCherry-GPI (Supplementary Fig. 11, Supplementary Movie 2), which also co-traffics with SM in secretory vesicles[17]. Overall, these results support a model in which phospholipids redistribute to the cytoplasmic leaflet during TGN vesicularization, while the luminal leaflet becomes enriched in newly synthesized sphingolipids (Fig. 3e). The resulting vesicles move both protein cargoes and asymmetrically-distributed lipids to the PM.

<u>PS asymmetry in the TGN is generated through lipid transport and flipping pathways</u>

269

270 Genetic evidence in yeast suggests that the asymmetry of PS in the vesiculated TGN could be
271 generated by P4-ATPase phospholipid flippases that translocate PS from the luminal leaflet to
272 cytoplasmic leaflet[42–46]. How asymmetry is generated in mammalian TGN has remained obscure
273 and it is unknown to what extent lipid flipping, or transport pathways at ER-TGN contact sites,
274 contribute to PS enrichment in the cytoplasmic leaflet (Fig. 4a). In mammalian cells, ORP10 and
275 ORP11 have recently been identified as ER-TGN transporters, where they shuttle PS from the
276 cytoplasmic leaflet of the ER to the cytoplasmic leaflet of the TGN through counter exchange of
277 phosphatidylinositol-4-phosphate[47–49]. Likewise, mammalian P4-ATPase phospholipid flippases
278 play important roles in maintaining PS asymmetry in the PM and secretory pathway[37,50–52].

279

280 To gain mechanistic insight into how PS asymmetry is generated at the TGN, we used FACES
281 to measure bilayer specific changes in N_3-PS distribution in cells silenced for either ORP9 and
282 ORP10, or the essential P4A-ATPase subunit CDC50a[53,54]. Silencing of ORP9, ORP10, and
283 CDC50a target genes was validated by western blot and resulted in >50% reduction in each
284 protein (Supplementary Fig. 12a-d). HeLa cells stably expressing GFP-TGN38-FAP oriented
285 toward the cytosolic leaflet were grown with 250 μM C-L-Ser-N_3 for 48 h during the siRNA
286 transfection. Silencing either ORP9 or ORP10 reduced **1a**-PS by 55% and 72%, respectively, on
287 the cytosolic leaflet of TGN vesicles compared to those treated with a non-targeted, negative
288 control siRNA (Fig. 4b). In comparison, silencing CDC50a reduced **1a**-PS by only 20% on the
289 cytosolic leaflet of TGN vesicles (Fig. 4c). Some cells silenced for CDC50a were also positive
290 for annexin V staining, indicating accumulation of extracellular PS in the PM (Supplementary
291 Fig. 12d). We thus tested whether silencing CDC50a would also cause PS accumulation in the
292 luminal leaflet of the TGN. Here it was necessary to increase C-L-Ser-N_3 labeling concentrations
293 to 500 μM to achieve adequate signal due to the low baseline abundance of N_3-PS in the

294 luminal leaflet. Under these conditions, we found that silencing CDC50a increased luminal
295 **1a**-PS content 2-fold in both TGN cisternae and vesicles (Fig. 4d). These results suggest that
296 cytosolic leaflet-to-leaflet lipid transport is a major driver of PS asymmetry observed in TGN
297 vesicles, while ATP-dependent flippases could have an additional role in maintaining
298 asymmetry.
299
300 FACES reports on changes to mitochondrial glycosylation dynamics
301
302 Based on our detection of surface glycans in the Golgi lumen, we asked whether FACES could
303 be used as a general tool compatible for imaging of azido-sugars in living cells.
304 *N*-azidoacetylgalactosamine-tetraacylated (Ac_4GalNAz) is widely used as a metabolic reporter
305 for glycoconjugates containing *N*-acetylhexosamines (HexNAz)[55]. Ac_4GalNAz fed to cells is
306 converted to UDP-*N*-azidoacetylgalactosamine (UDP-GalNAz) by the hexosamine salvage
307 pathway and is then further epimerized to UDP-*N*-azidoacetylglucosamine (UDP-GlcNAz) (Fig.
308 5a). This results in robust labeling of *N*- and *O*- linked glycoproteins on the cell surface[55,56] (Fig.
309 5b), secretory compartments where they are formed, and endosomal compartments where they
310 are recycled. Meanwhile, intracellular protein glycosylation is modulated by nucleocytoplasmic
311 and mitochondrial *O*-linked β-*N*-acetylglucosamines (*O*-GlcNAc), which are added to
312 serine/threonine residues by *O*-GlcNAc transferase (OGT) and removed by *O*-GlcNAcase
313 (OGA)[55] (Fig. 5c). *O*-GlcNAc cycling has emerged as a regulator of metabolism, signaling, and
314 immune evasion of cancer cells[57–59] and mitochondrial motility in neurons[60]. However,
315 intracellular glycosylations are not readily observed by standard bioorthogonal imaging
316 approaches due to the much more extensive incorporation of Ac_4GalNAz into surface glycans;
317 very little signal from conjugated conventional fluorophores co-localizes with mitochondria, for
318 example (Fig. 5d). Currently, detection of *O*-GlcNAcylation is performed in fixed cells or bulk
319 extracts using *O*-GlcNAc sensitive antibodies[61].

320

321 Using MTS-FAP-GFP expressing cells, we tested the efficacy of FACES in reporting
322 mitochondrial-specific changes in HexNAz. Cells were grown in the presence or absence of
323 either 100 μM Ac_4GalNAz or 100 μM *N*-azidoacetylglucosamine-tetraacylated (Ac_4GlcNAz) for
324 24h. Ac_4GlcNAz is not efficiently incorporated by the hexosamine salvage pathway[55] and thus
325 was used as a less metabolically active surrogate. SPAAC staining with **1b** generated
326 fluorescence signal intensities 10-fold greater in cells fed 100 μM Ac_4GalNAz compared to unfed
327 control cells (Fig. 5e). In contrast, **1b** fluorescence from cells fed Ac_4GlcNAz, which is less
328 efficiently incorporated into glycosylated proteins, was significantly lower than that for
329 Ac_4GalNAz, indicating that the FACES signal from **1b**-HexNAz is from sugars that have been
330 metabolically incorporated and not due to free azido sugars.

331

332 Next we tested whether FACES can report changes to mitochondrial *O*-GlcNAc levels resulting
333 from pharmacological treatment or nutritional state. We found that the OGA inhibitor Thiemet-G
334 increased **1b**-HexNAz fluorescence, suggesting that the fluorogen signal was responsive to the
335 activity of *O*-GlcNAc modifying enzymes (Fig. 5f). In cancer cells, glucose uptake is positively
336 correlated with *O*-GlcNAc levels, which in-turn reprogram cellular metabolism tailored towards
337 glucose availability[62]. We observed that switching cells from high (30 mM) to low glucose (5.5
338 mM) levels during Ac_4GalNAz labeling reduced **1b**-HexNAz fluorescence by 30% (Fig. 5g). This
339 is similar to glucose-dependent changes in mitochondrial *O*-GlcNAc levels previously reported
340 in breast cancer cells[63]. Taken together, these data demonstrate that FACES can report
341 changes in mitochondrial HexNAz incorporation as a function of cell metabolism and
342 *O*-GlcNAcylation in living cells, and support the hypothesis that mitochondrial *O*-GlcNAcylation
343 is a post-translational modification that is responsive to the cell's dietary state.

344

345

Discussion

Studying cellular roles for non-proteinaceous biomolecules has long been hindered by the lack of robust tools for their imaging in live cells. Here we introduce a new approach, FACES, that combines the chemical specificity of metabolic incorporation with the spatial control of genetic protein tagging for imaging of cellular metabolites. FACES harnesses reversible fluorogenic systems, where fluorescence increases many orders of magnitude upon specific binding to a FAP. It combines this turn on fluorescence with the specificity of bioorthogonal reactions for molecular sensing. This approach is powerful for the subcellular imaging of phospholipids, their transport between organelles, and orientations across membrane leaflets, but can also be applied to other biomolecules. Metabolic labeling has emerged as a particularly important tool for glycobiology and we demonstrate that FACES is responsive to labeled glycoproteins in mitochondria, which have been proposed to act as regulators of metabolic function[64]. Future applications of FACES could be further expanded through increases in the repertoire of metabolic labeling, bioorthogonal chemistry, and the spectral plasticity of the fluorogen employed.

Compared to other bioorthogonal imaging modalities, FACES has several key advantages for mechanistic lipid membrane biology. For organelle-defined imaging, protein targeting sequences are more specific and generalizable than corresponding chemically-encoded localization tags. We show that this capacity can be applied to the quantitative characterization of lipid distribution phenotypes affected by trafficking networks across membrane contact sites. Beyond organelle-specific imaging, FAPs can also be fused to specific TMDs to read out bilayer asymmetry. Here, FACES provides effective discrimination beyond what is possible with direct fluorescence imaging, as the distance between two bilayer leaflets is less than 4 nm. Fluorogens show no fluorescence when unbound to their corresponding FAP, so quantitative

372 detection of conjugate products occurs through the resulting fluorescence signal, not a change
373 in its localization as for lipid binding proteins. Because of this capacity, FACES is the only
374 method, to our knowledge, that allows for measurement of membrane asymmetry in live cells.
375
376 Applications of FACES could be further expanded through increases in the repertoire of
377 metabolic labeling, bioorthogonal chemistry, and the spectral plasticity of the fluorogen
378 employed. Conjugation of fluorogens to biomolecules is dependent on tagged metabolite
379 incorporation, which are continuously expanding across biological systems[65] and molecular
380 classes[66]. One concern with any metabolic labeling approach is that tagged molecules might not
381 fully mimic native compounds, which is especially relevant for lipids with minimal headgroups.
382 For several azido lipids, previous studies suggest that compounds localize across a range of
383 cells as expected[10,11], though it is challenging to preclude all differences between labeled and
384 unlabeled species. An additional limitation common to bioorthogonal approaches is the time
385 required for conjugation and washing out of unreacted fluorogens; these might make the
386 analysis of rapid redistributions of the underlying labeled species, like those relevant for lipid
387 signaling[67], challenging. Tuning fluorogenic reagents for faster conjugations[68] and washing could
388 decrease the time for processing steps to capture dynamic distributions.
389
390 Our experiments demonstrate that FACES is an especially powerful tool for investigating cellular
391 mechanisms by which lipids are transported between organelles and across individual
392 membranes, an intense area of investigation. A plethora of shuttle and bridge-like LTPs that
393 perform lipid exchange at contact sites[6] and flippases/floppases/scramblases that act on bilayer
394 asymmetry[69] have been identified and biochemically tested. However, these transporters are
395 characterized by overlapping affinities, apparent redundancies, and close interactions with lipid
396 metabolic enzymes; how they act in concert to shape the membrane heterogeneity that defines
397 eukaryotic cells is still unknown. Here, we identify transporters that contribute to the asymmetry

398 of several labeled phospholipid classes at the TGN. The Golgi has long been proposed as a site
399 of asymmetry generation, given the co-occurrence of secretory cargo sorting to the PM and
400 sphingolipid synthesis[70]. We show that for one phospholipid class, PS, cytosolic LTPs and
401 transbilayer flippases both contribute to the striking asymmetry observed in TGN vesicles.
402 These secretory compartments are enriched in GPI-anchored secretory cargoes that associate
403 with the exoplasmic leaflet of the PM, suggesting a mechanism by which asymmetry at the PM
404 is generated earlier in the secretory pathway. Lipid asymmetry generated at the TGN could also
405 be relevant for sorting membrane proteins based on the asymmetric TMD sequences that are
406 required for their PM targeting[3,71]. As a tool that provides spatially-defined molecular
407 quantitation, FACES could be broadly powerful for untangling how lipid trafficking, generation of
408 membrane asymmetry, and transport of cargoes occurs throughout eukaryotic cells.
409

410 **Acknowledgements**

411

412 Nicolas-Frédéric Lipp provided discussions and comments, Gulcin Perkunnaz provided
413 discussions and reagents, Jennifer Santini and the UCSD Microscopy Core (NS047101,
414 OD030505) provided assistance with microscopy, Chris Burd and Jennifer Lippincott-Schwartz
415 provided plasmids. The work was supported by the National Institutes of Health
416 (R35-GM142960 to I.B. and R35-GM141939 to N.K.D.) and the National Science Foundation
417 (CHE-2310263 to M.D.B.). R.J.B. acknowledges Agencia Estatal de Investigación and the
418 Ministerio de Ciencia e Innovación (RYC2020-030065-I). The global polar phospholipid
419 analyses described in this work were performed at the Kansas Lipidomics Research Center
420 Analytical Laboratory. Instrument acquisition and lipidomics method development were
421 supported by the National Science Foundation (including support from the Major Research
422 Instrumentation program; most recent award DBI-1726527), K-IDeA Networks of Biomedical
423 Research Excellence (INBRE) of National Institute of Health (P20GM103418), USDA National

Institute of Food and Agriculture (Hatch/Multi-State project 1013013), and Kansas State University."

Methods

Synthesis of fluorogen reagents: Synthesis schematic of compounds **1a** and **1b** are shown in Supplementary Fig. 1 and synthetic protocols are detailed in the Supplementary Text. Products were validated by LC-MS and $^{1}H/^{13}C$ NMR.

Generation of constructs: FAPs were cloned from pcDNA3.1-KozATG-dH6.2-2XG4S-actin[21], pcDNA3.1-kappa-myc-dK-2xG4S-TMst[72], and pcDNA3.1-kappa-myc-dL5-2XG4S-mCer3-KDEL[73] (Addgene). These FAP sequences and the pcDNA3.1 backbone were used for generating the FAP-GFP-KDEL, GFP-KDEL, and MTS-FAP-GFP constructs used in transfection experiments. The Ig Kappa secretion signal was used in conjunction with a KDEL sequence for ER-targeted constructs, while the targeting sequence from OTC was used for MTS constructs. For stable expression, FAP-GFP-KDEL and MTS-FAP-GFP coding sequences were subcloned into the sleeping beauty expression vector SBbi-PUR[74] (Fig. 2, Fig. 5, Supplementary Fig. 6). Constructs utilizing TGN38 were derived from mCer3-TGN38, which was a gift from the Lippincott-Schwartz lab. In transfection experiments, the dH6.2 sequence was inserted into either the N-terminal or C-terminal side of the TGN38 transmembrane domain to generate mCer3-FAP-TGN38 and mCer3-TGN38-FAP constructs, respectively (Fig. 3d, Supplementary Fig. 9, Supplementary Fig. 10, Supplementary Fig. 11). For stable cell lines, a reciprocal tagging approach was taken to generate FAP-TGN38-GFP and GFP-TGN38-FAP constructs assembled into the SBtet-Pur expression vector (Fig. 3, Fig. 4, Supplementary Fig. 8). The GPI-anchor marker protein was generated by subcloning a mCherry-SBP-GPI sequence, received from the Lippincott-Schwartz lab, into pcDNA3.1. The GFP-EqtSM plasmid was received as a gift from

450 the Burd lab. Additional Sec61mCherry and Mito-BFP plasmids were received from the
451 Lippincott-Schwartz lab. All constructs were validated by whole plasmid sequencing.
452
453 Cell culture: HeLa (ATCC CCL-2) cells were grown in Dulbecco's Modified Eagle Medium
454 (Gibco 11995-065) containing glucose (4.5 g/L), glutamine (4.5 g/L), sodium pyruvate (110
455 mg/L), phenol red, 10% FBS, and 1% PenStrep, at 37°C and 5% CO_2 atmosphere. For
456 microscopy, cells were seeded into 35 mm glass bottom dishes (MatTek) coated with fibronectin
457 (7.5 µg/mL). For transient expression, cells were transfected with Lipofectamine 3000 in
458 Opti-MEM media for 4 h, and changed into normal growth medium containing azido-containing
459 bioorthogonal metabolite for 24 h prior to SPAAC labeling and imaging. Stable cell lines
460 expressing FAPs were generated using the Sleeping Beauty transposon insertion system. After
461 transfection, cells were grown under selection with puromycin (10 µg/mL) for 2 weeks until all
462 showed fluorescence. Doxycycline (1 µg/mL) was used to induce expression in
463 SBtet-FAP-TGN38-GFP, SBtet-GFP-TGN38-FAP, and SBtet-mCer3-TGN38-FAP cell lines (Fig.
464 3, Fig. 4, Supplementary Fig. 8, Supplementary Fig. 10). Cells were routinely tested for
465 mycoplasma by MycoStrip (InvivoGen).
466
467 Metabolic labeling: 1-azidoethyl-choline (N_3-Cho, Jena BioScience) and resuspended in PBS to
468 stock concentration of 50 mM. Ac_4ManNAz, Ac_4GalNAz and Ac_4GlcNAz (Click Chemistry Tools)
469 were resuspended in DMSO to stock concentration of 100 mM. L-Serine analogue C-L-Ser-N_3
470 and *myo*-Inositol analogue Inos-N_3 were synthesized as previously reported, verified by $^1H/^{13}C$
471 NMR and high resolution mass spectrometry, and resuspended in PBS to a stock concentration
472 of 50 mM and 100 mM, respectively. In all cases, metabolic incorporation occurred for 24 h,
473 except for experiments in Fig.4, which occurred for 48 h. Afterwards, cells were washed once
474 with HBSS buffer, and incubated in fresh growth media for 30 min to allow for metabolic

475 consumption of any remaining bioorthogonal metabolites. For experiments with peracetylated
476 sugars, 1 h incubation was used.
477
478 SPAAC conjugation: Culture media was removed by aspiration and replaced with staining media
479 for SPAAC labeling. The staining media contained 500 nM **1a** or **1b** diluted in serum-free DMEM
480 clear (Gibco 31053-028), and incubated for 15-20 min at 37°C and 5% CO_2 atmosphere. Cells
481 were washed with 4 volumes of culture media containing 10% FBS, 3 times, at 15 min intervals
482 to remove unreacted dye. For experiments with the mitochondrial-localized FAP, cells were
483 incubated for an additional 45 min, followed by a fourth wash step prior to imaging.
484
485 Lipid analysis: Lipids were extracted with a modified Bligh and Dyer protocol. Briefly, cell pellets
486 from T75 culture flasks were resuspended in 200 µL PBS and extracted with 2 mL 1:2
487 $CHCl_3$:MeOH (v/v) and cell debris were removed by centrifugation. Extracts were transferred to
488 new vials and 1 mL chloroform was added, followed by 1 mL H_2O, and shaking. The lower
489 organic phase was collected after centrifugation and the aqueous phase was extracted twice
490 more with 650 µL and pooled. Lipid extracts were then dried under N_2 and resuspended in 100
491 µL 1:2 $CHCl_3$:MeOH for thin-layer chromatography (TLC) and 500 µL methanol for LC-MS/MS.
492 For TLC, entire lipid extracts were spotted onto 10x10 cm HPTLC silica gel 60 plates,
493 developed with 14:5:1 $CHCl_3$:MeOH:NH_4, and imaged with a Typhoon FLA 9500 using 633 nm
494 laser. For high resolution LC-MS/MS, 5 µL sample was injected, andHRMS spectra of the total
495 lipid extracts from HeLa cells were recorded on a Q Exactive Orbitrap mass spectrometer
496 (Thermo Fisher Scientific) connected to a Vanquish Flex Analytical UHPLC System (Thermo
497 Fisher Scientific) equipped with a C8 column (100 x 2.1 mm, particle size 1.9 µm). Following
498 HPLC method was used for all runs using 0.1% formic acid in water (Solvent A) and 0.1%
499 formic acid in methanol (Solvent B): 0-1 min 30% B, 1-4 min 30%-90% B, 4-15 min 90-99% B,
500 15-18 min 99%B, 18-20 min 30% B. Lipid standards (POPC, N_3-DSPC) were supplied by Avanti

501 Polar Lipids. Global polar phospholipid analysis was performed by ESI-MS/MS at the Kansas
502 State Lipidomics Research Center as previously described[75–77].
503
504 Image collection: Confocal micrographs were acquired on a Zeiss LSM 880 microscope
505 equipped with plan-apochromat 64x/1.4 NA or 20x/0.8 NA objectives. For far-red fluorogen-FAP
506 signals, a 633 nm HeNe laser was used at 1-2% power. FP or other fluorophores were excited
507 with 488 nm Argon (GFP), 405 nm (BFP/mCer3) or 561 nm (mCherry) diode lasers. All images
508 used for intensity quantification were acquired in LSM mode using a QUASAR GaAsP detector
509 using identical settings. Images highlighting fluorogen distribution (Figs. 2a, 2b, 3b, 3d;
510 Supplementary Figs. 3, 9, 10, 11; Supplementary Movies 1, 2) were acquired with an Airyscan
511 detector and processed using default settings in Zen Black; these were not used for
512 quantification due to non-linear processing. SIM imaging of mitochondrial **1b**-PC was
513 performed on an Zeiss Elyra 7 Lattice-SIM^2 system equipped with a plan-apochromat 100x/1.46
514 NA objective using 642 nm and 488 nm diode lasers (10% power each). Images were acquired
515 in ZEN Black using Weak Live default settings with a pixel dwell time of 843 ms.
516
517 Image quantification: All intensity were calculated using ImageJ on unprocessed images. For
518 proof of concept experiments using transfected cells (Fig. 1), line profiles drawn were across 10
519 individual ER segments per cell and the total fluorescence ratio between fluorogen and GFP
520 emissions were tabulated across them. For per-cell data (Fig. 1f, 1h), the 10 segments were
521 averaged and 10 cells were analyzed per condition. Raw per segment fluorescence intensity is
522 shown for all 100 segments (Fig. 1g). For mitochondrial and ER quantification (Fig. 2), fields of
523 cells stably expressing to corresponding FAPs were analyzed by segmenting individual cells
524 and computing the total fluorescence ratio between fluorogen and GFP emission across the
525 entire cell, given the highly specific distribution of the signal for the compartment of interest. For
526 TGN cisternae quantification (Fig. 3, Fig. 4), line segments were drawn across the Golgi

527 apparatus of individual cells so that they did not intersect any TGN vesicles. For TGN vesicle
528 quantification, 5 line segments were drawn across Golgi vesicles that did not intersect Golgi
529 cisternae. For each compartment, the total fluorescence ratio between fluorogen and GFP were
530 calculated across each and averaged together for a single cell value. Values were measured
531 this way for 25 cells per condition (luminal vs. cytosolic for PC, PS, PI, and SiA). Mitochondrial
532 quantification in Fig. 5 was carried out identically as in Fig. 3. All statistical analyses were
533 performed in GraphPad Prism 9.
534
535 Gene knockdown: Silencer Select siRNAs were supplied by Thermo Fisher: STARD7 (s32370),
536 VPS13a (s531256), ORP9 (s41693), ORP10 (s223235), CDC50a (s31427), and negative
537 control 1 (4390843). Cells were transfected with Lipofectamine RNAiMAX (ThermoFisher)
538 complexed with 25 pmol siRNA for 48h prior to analysis. 50 pmol siRNA was used for CDC50a.
539 Total protein was extracted using RIPA Lysis and Extraction buffer (ThermoFisher) and
540 measured by Bradford assay (Bio-Rad). A total 20 µg protein per extract was boiled in 1X
541 reducing sample buffer and used for SDS-PAGE (BioRad, 4561083). Validation of gene
542 knockdowns was performed by Western blotting using primary antibodies against STARD7
543 (Proteintech, 15689) 1:2500, VPS13a (Atlas antibodies, HPA021662) 1:1000, ORP9
544 (Proteintech, 11879-1-AP), ORP10 (Proteintech, 15491-1-AP), CDC50a (Invitrogen,
545 PA5-99762), and Actin (Invitrogen, PA5-78715) 1:5000. HRP-conjugated goat anti-rabbit IgG
546 secondary antibody (Abcam, 6721) 1:10,000 and Pierce ECL western blotting substrate
547 (Thermo Fisher, 32209) were used for detection.
548
549
550

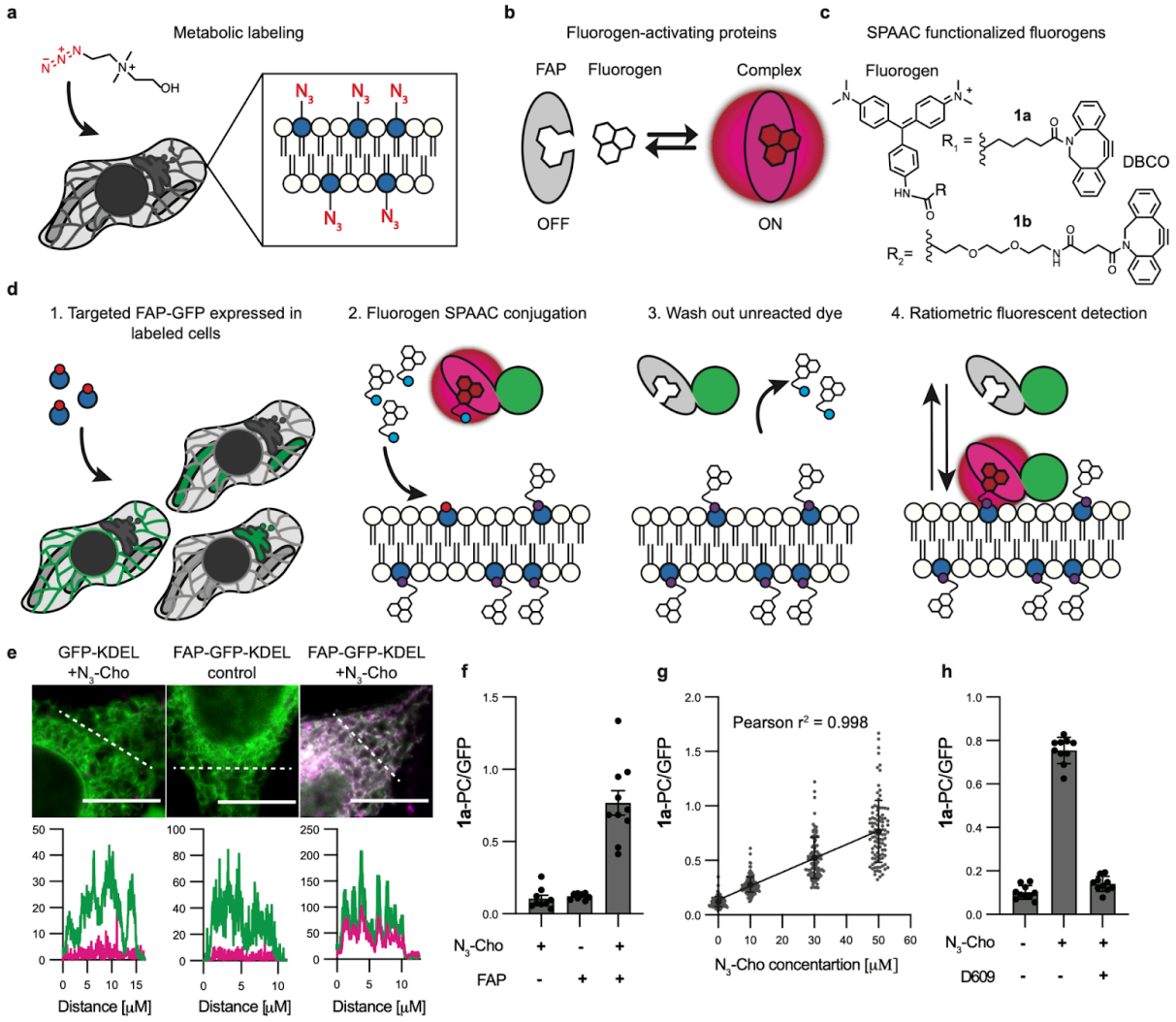

Figure 1. Conceptual development of FACES

a, N_3-Cho is metabolically incorporated into azido-PC lipids distributed throughout all cellular membranes. **b,** Fluorogens form reversible non-covalent fluorescent complexes with genetically encoded FAPs. **c,** Structure of the fluorogen malachite green linked to dibenzocyclooctyne for SPAAC labeling. **d,** Conceptual schematic detailing the FACES method. (1) Cells expressing a FAP-GFP fusion protein targeted to an organelle of interest are metabolically labeled with N_3-Cho, or other bioorthogonal metabolite. (2) After incorporation, metabolites are conjugated via a SPAAC reaction with fluorogen-DBCO. During this time free dye can interact with the FAP to generate far-red fluorescence. (3) After SPAAC labeling, excess free dye is reversibly disassociated from the FAP complex and removed from cells by washing. (4) Subsequent imaging of the fluorogen-FAP complex is used to detect the specific biomolecule pool.

Co-measurement of GFP fluorescence is used to normalize the fluorogen signal to FAP sensor density. **e,** Merged confocal images of transfected HeLa cells post washing. White line indicates the segment used for plotting the fluorescent intensity profile of **1a** and GFP shown below. Scale = 10 μm. **f,** Quantified fluorescence intensity profiles from confocal images expressed as ratiometric average; *n* = 10 cells. **g,** Linear regression of quantified fluorescence from transfected HeLa cells fed 0, 10, 30, 50 μM N_3-Cho and labeled with 500 nM **1a**; *n* = 100 individual ER segments derived from 10 cells. **h,** Quantified fluorescence of cells incubated with the PC synthesis inhibitor D609 alongside N_3-Cho; *n* = 10 cells.

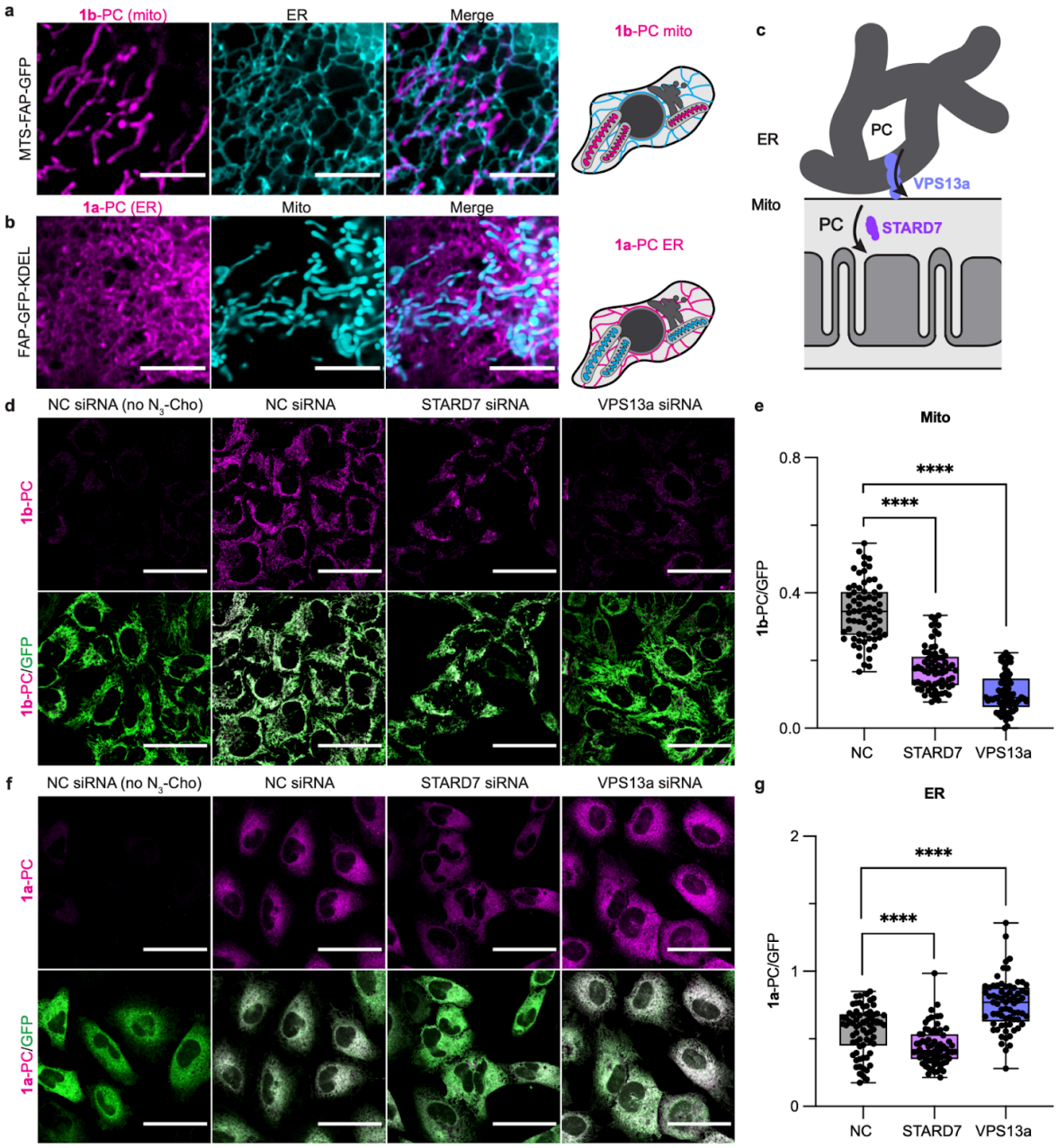

Figure 2. Using FACES to analyze PC trafficking between the mitochondrion and the ER **a,** HeLa cells co-transfected with a mitochondrial matrix FAP (MTS-FAP-GFP) and an ER marker (Sec61b-mCherry) show **1a**-PC fluorescence that does not overlap with the ER. **b,** HeLa cells co-transfected with an ER-localized FAP (FAP-GFP-KDEL) and a mitochondrial marker (mito-BFP) show **1a**-PC fluorescence in the far-red channel that does not overlap with mitochondria. For both **(a)** and **(b)**, 50 μM N_3-Cho and 500 nM **1a** were used for PC labeling, Scale = 5 μM. **c**, Cartoon schematic depicting two proposed modes of PC transport into mitochondria. **d-g**, Knockdown of two putative ER-mitochondrial lipid transporters alters the

distribution of PC between the two organelles. **d** and **f**, Representative LSM images of siRNA transfected HeLa cells stably expressing either MTS-FAP-GFP (**d**) or FAP-GFP-KDEL (**f**). Scale = 50 μm. **e** and **g**, Quantified fluorescence intensity ratios of fluorogen to GFP. Values were normalized to the average background fluorescence in NC siRNA (no N_3-Cho) control cells. 100 μM N_3-Cho was used for PC labeling with either 500 nM **1a** (ER) or **1b** (Mito). *n* = 69 cells per condition; ****, $p < 0.001$, as determined by Student's t-test.

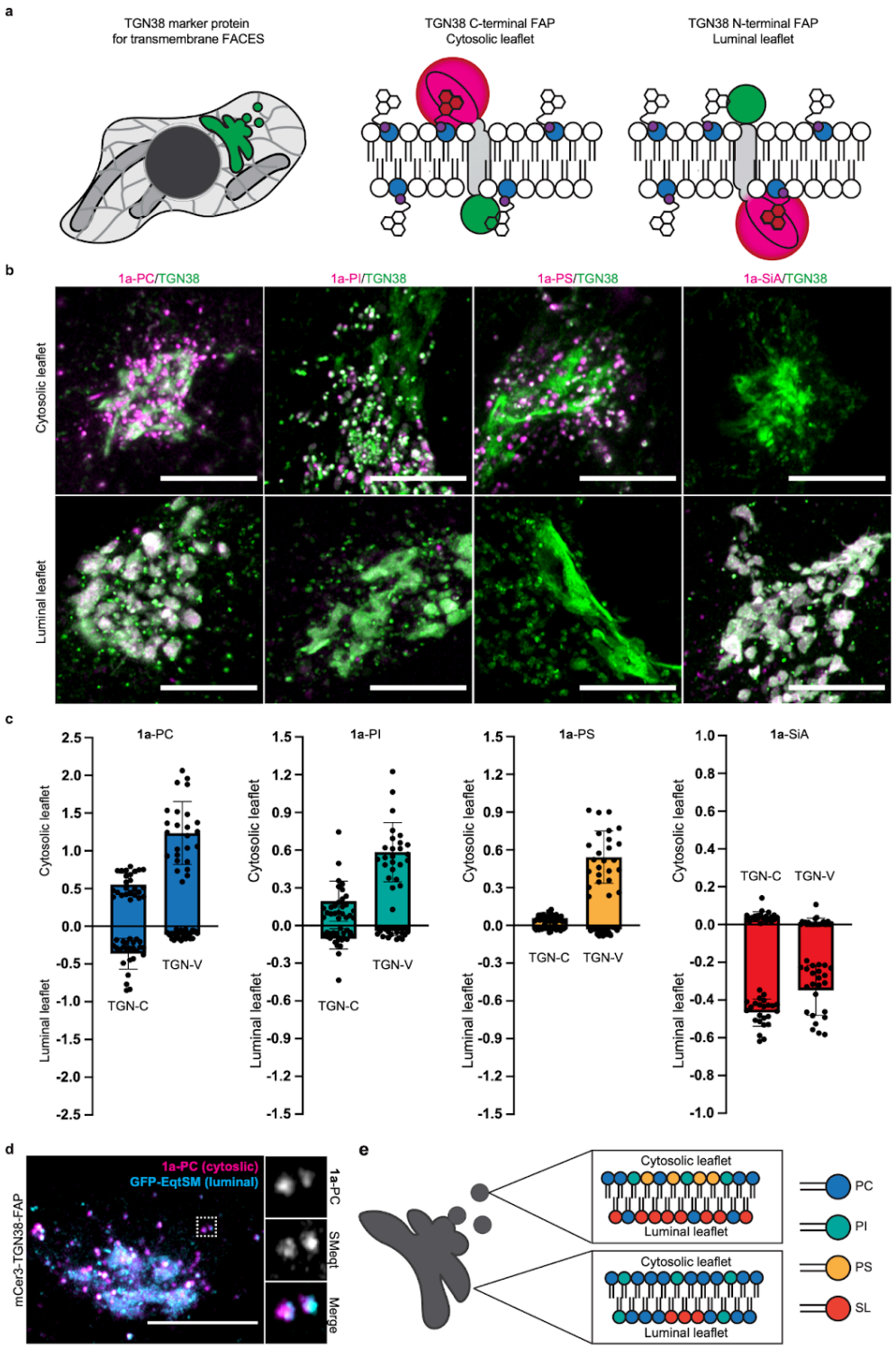

Figure 3. Imaging lipid asymmetry generated at the TGN with FACES

a, Illustrated schematic representing the constructs used for reciprocal tagging of TGN38 with a FAP exposed to the cytosolic or luminal leaflet. The constructs also include the green

fluorescent protein GFP on the opposing leaflet to account for sensor abundance. **b,** Example composite images of individual Golgi from HeLa cells stably expressing the cytosolic (top) or luminal (bottom) TGN38 FAP sensors. Cells were treated with a tracer for PC (100 μM N_3-Cho), PI (50 μM Inos-N_3), PS (250 μM C-L-Ser-N_3), or Sia (50 μM Ac_4ManNAz). Images were acquired using 488 nm and 633 nm laser lines. Magenta regions are enriched in the fluorogen conjugated metabolite, green regions correspond to low metabolite levels, while white regions show intermediate values, relative to the sensor levels. Scale bar = 10 μm. **c**, Quantification of the fluorescence intensity ratio of fluorogen to GFP for each metabolite and each orientation (cisternae, TGN-C; vesicles, TGN-V). Values were calculated post-subtraction of the background fluorescence using unfed null controls. Error bars indicate SD; *n* = 25 cells per metabolite per leaflet. Raw values and statistical analyses are provided in Supplementary Fig. 8. **d**, Co-localization of SMeqt-GFP and cytoplasmic **1a**-PC in individual TGN vesicles, as detected by mCer3-TGN38-FAP. Here, 488 and 633 nm laser lines were used for imaging to avoid imaging of mCer3. The SMeqt-GFP channel is colored cyan and the **1a**-PC channel is colored magenta. Scale = 10 μm. **e,** Conceptual model representing the proposed asymmetric distribution of PC and SM lipids that is generated alongside TGN vesicle formation.

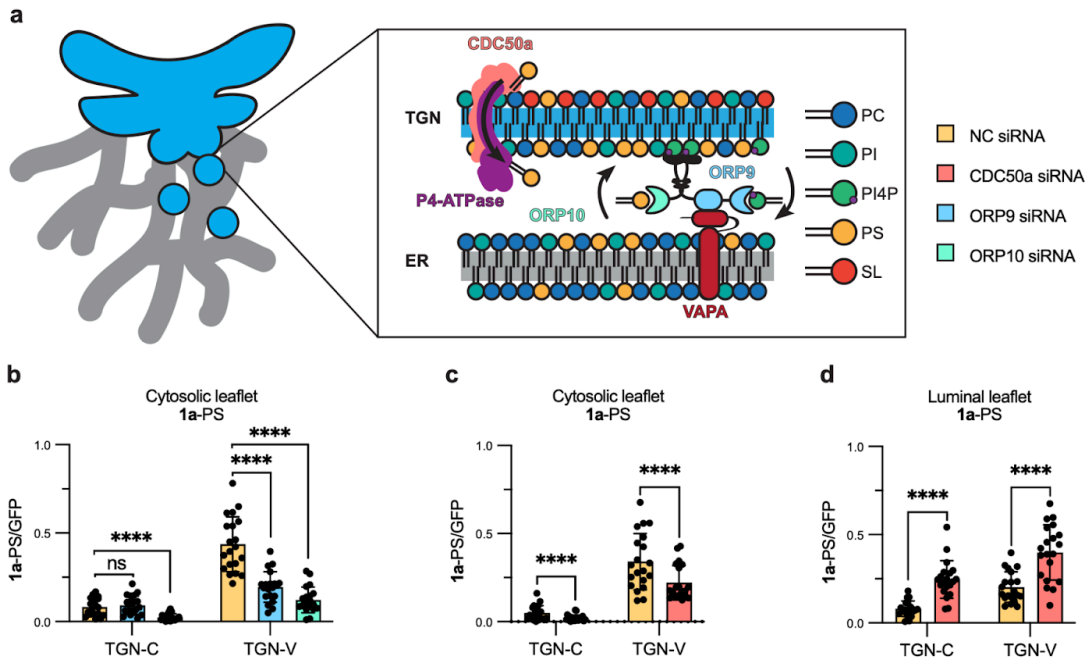

Figure 4. Mechanisms contributing to PS asymmetry at the TGN

a, Cartoon schematic depicting two proposed lipid transport pathways generating PS asymmetry at the TGN. PS can be flipped from the luminal leaflet to the cytoplasmic leaflet of the TGN by P4-ATPase/CDC50a flippases or transported from the cytoplasmic leaflet of the ER to the cytoplasmic leaflet of the TGN by ORP9/10/11 LTPs at contact sites with VAPA. **b** and **c**, Quantified ratio of **1a**-PS to GFP fluorescence in the cytoplasmic leaflet of the TGN in response to siRNA transfection. **b**, ORP9 (blue) and ORP10 (green) silencing reduce **1a**-PS relative to cells treated with a negative control (NC) siRNA (orange). **e**, Silencing CDC50a (red) also decreases **1a**-PS in the cytoplasmic leaflet, but by a smaller amount. Cells were fed 250 μM C-L-Ser-N_3 during the 48 h siRNA transfection period and labeled with 500 nM **1a**. **d**, Silencing CDC50a increases **1a**-PS in the luminal leaflet of the TGN d relative to NC siRNA treated cells. Cells were fed 500 μM C-L-Ser-N_3 during the 48 h siRNA transfection period and labeled with 500 nM **1a**. Values have been normalized to the average background signal from NC siRNA cells that were not fed C-L-Ser-N_3 as a staining control. Error bars indicate SD. In all experiments n = 20 cells per condition; ****, $p < 0.0001$, as determined by Student's t-test.

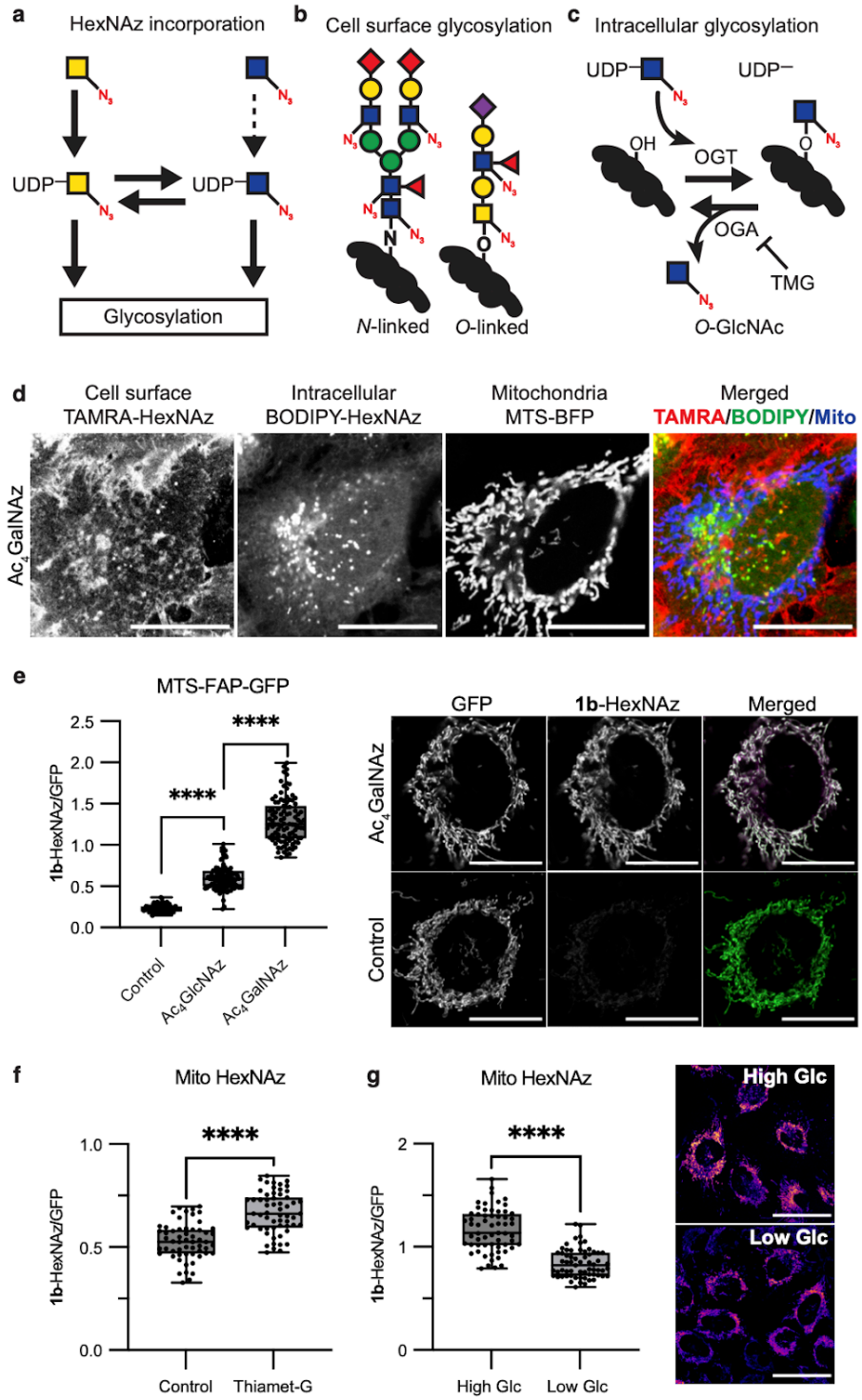

Fig. 5. Intracellular imaging of *N*-acetylhexosamine sugars with FACES

a, Illustration depicting the metabolic fate of Ac_4GalNAz (yellow square) and Ac_4GlcNAz (blue square) incorporation into cellular glycoconjugates containing *N*-acetylhexosamine sugars.

641 Ac_4GalNAz fed to cells is converted to UDP-GalNAz in the cytosol and further epimerized to
642 UDP-GlcNAz, thereby robustly labeling both UDP-HexNAz pools (UDP-GalNAz +
643 UDP-GlcNAz). Conversely, Ac_4GlcNAz is not efficiently recycled to UDP-GlcNAz. **b**,
644 UDP-HexNAz is incorporated into diverse extracellular glycoproteins proteins on the cell
645 surface. Structures for an *N*-linked glycoprotein and *O*-linked mucin are shown as examples. **c**,
646 UDP-HexNAz is incorporated into intracellular *O*-GlcNAcylated proteins. Protein glycosylation is
647 catalyzed by *O*-GlcNAc Transferase (OGT) and can be reversed by *O*-GlcNAcase (OGA). OGA
648 is pharmacologically inhibited by Thiamet-G (TMG). **d,** Bioorthogonal imaging of HeLa cells fed
649 100 μM GalNAz for 24h and labeled with 5 μM TAMRA-DBCO (cell surface) and 5 μM
650 BODIPY-DBCO (intracellular), relative to the mitochondrial marker Mito-BFP. Scale = 20 μm. **e-i**,
651 Stable MTS-FAP-GFP cells detect mitochondrial HexNAz. **e**, Quantified mitochondrial HexNAz
652 incorporation in cells fed either 100 μM Ac_4GalNAz or 100 μM Ac_4GlcNAz for 24h, versus unfed
653 controls. Error bars indicate SD; *n* = 100 cells. Cells were labeled with 500 nM **1b** and washed
654 as previously described. Representative images of Ac_4GalNAz fed cells and control are shown
655 on the right; scale = 20 μM. **f**, Response of mitochondrial HexNAz to OGA inhibition using
656 Thiamet-G (TMG). Cells were treated with 50 μM Thiamet-G (or DMSO control) and fed 100 μM
657 Ac_4GalNAz for 24h. Displayed values are normalized to the average background fluorescence
658 of unfed cells, which were used to control for **1b** labeling. Error bars indicate SD; *n* = 59 cells. **g**,
659 Response of mitochondrial HexNAz to glucose availability. Cells were fed 100 μM Ac_4GalNAz
660 and grown in DMEM containing either low (5.5 mM) or high (30 mM) glucose for 24h. Displayed
661 values are normalized to unfed cells used as control for **1b** labeling. Error bars indicate SD; *n* =
662 63 cells. Representative LSM images (right) show **1b**-HexNAz fluorescent intensities displayed
663 using the FireLUT. Scale = 50 μm.
664
665

Supplementary Figures

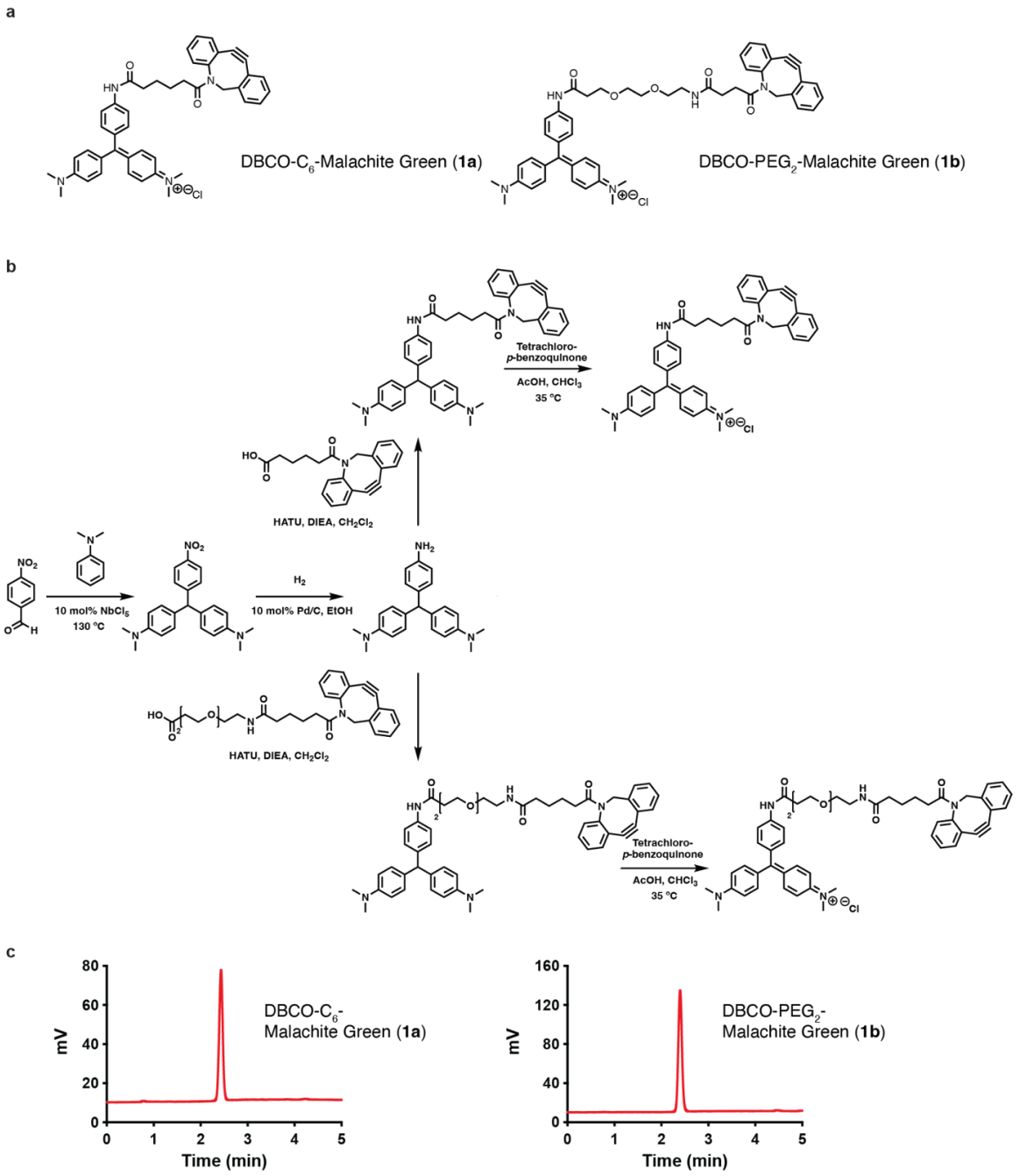

Supplementary Fig. 1. Synthesis of DBCO-linked fluorogens

a, Chemical structures of all the Malachite Green (Chromatic forms) derivatives used in this study. **b**, Synthesis of the chromatic forms of DBCO-C_6-Malachite Green (**1a**) and DBCO-PEG_2-Malachite Green (**1b**). **c**, HPLC/ELSD spectrum corresponding to the chromatic forms of DBCO-C_6-Malachite Green (**1a**) and DBCO-PEG_2-Malachite Green (**1b**). Retention times were verified by mass spectrometry.

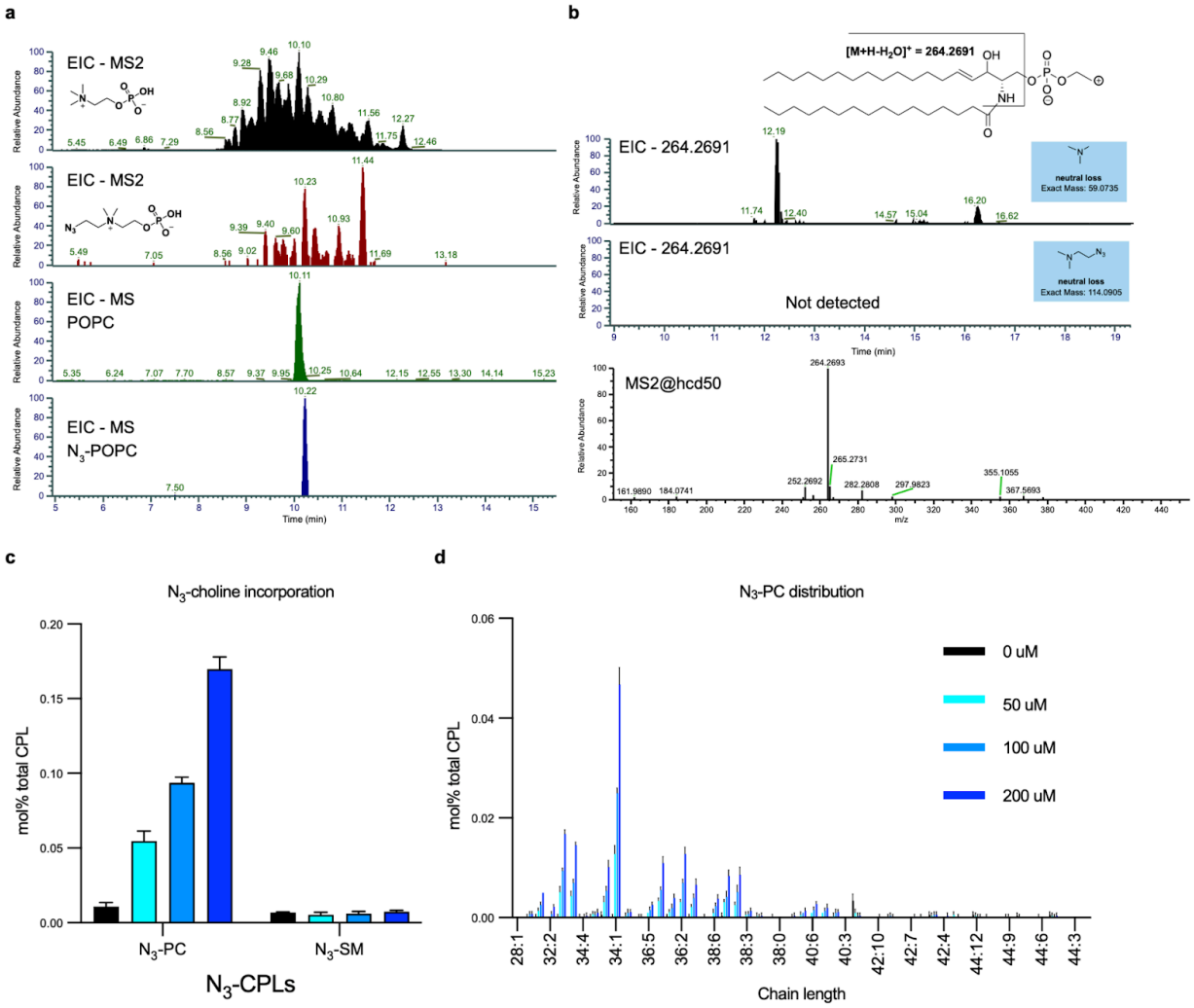

Supplementary Fig. 2. N_3-Cho is metabolized into N_3-PC but not N_3-SM

a and **b**, Cells were fed 100 μM N_3-Cho for 24 h and extracted lipids were analyzed by LC-MS/MS. **a**, Comparative extracted ion chromatograms (EIC) from full scan/all ion fragmentation mode. MS2 fragments: choline (black), N_3-Cho (red). EIC of POPC (green) and N_3-POPC (blue) were detected as representative PC species in the sample. **b**, Sphingoid base fragment 264.269 was detected in neutral loss scan mode NL = 59 (choline containing lipids) but not in NL = 114 (N_3-Cho containing lipids), indicating N_3-Cho was not incorporated into SM in a detectable amount under these labeling conditions. **c**, Quantification of N_3-Cho incorporation into N_3-PC and N_3-SM by ESI-MS/MS. **d**, Distribution of N_3-PC species by acyl chain length and saturation.

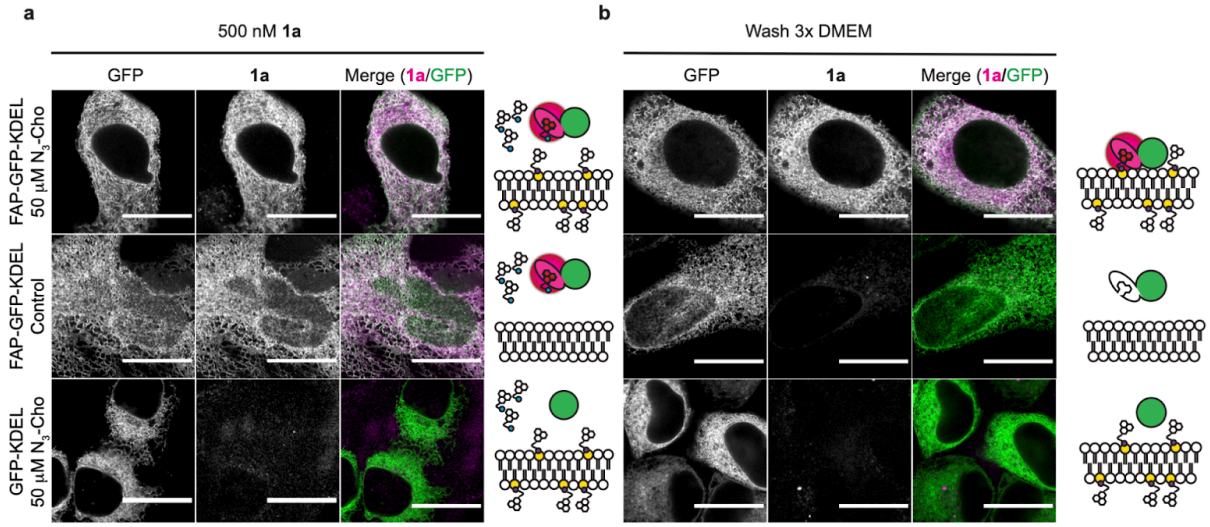

Supplementary Fig 3. Imaging N_3-PC in the ER using compound 1a

a, b, HeLa cells transfected with either FAP-GFP-KDEL (top two rows) or GFP-KDEL (bottom row) were grown in the presence (top and bottom rows) or absence (middle row) of 50 μM N_3-Cho and labeled with 500 nM **1a**. Cells were imaged while in the labeling solution **(a)** and after washing with culture medium **(b)**. Scale = 20 μm.

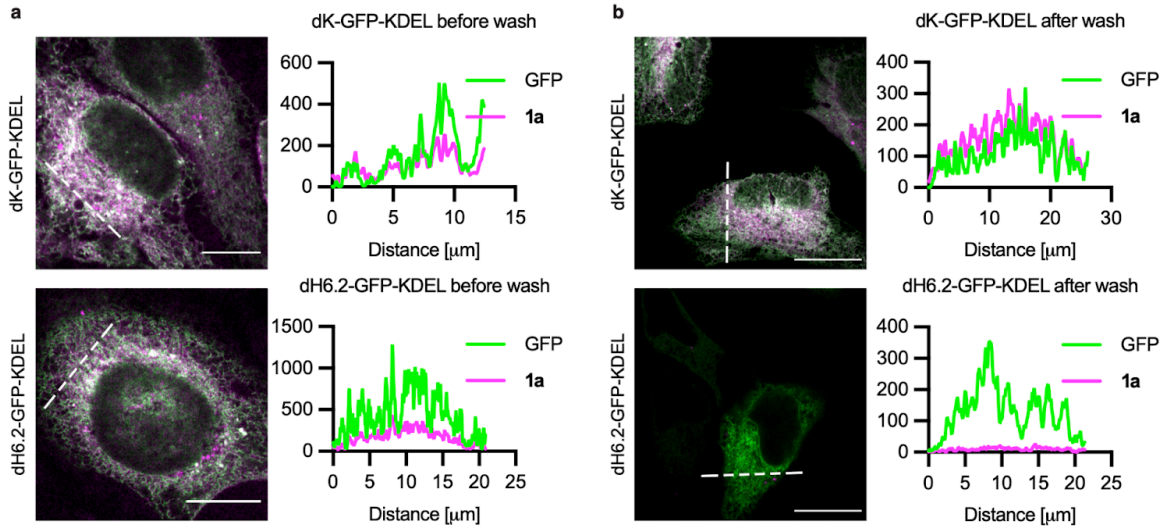

Supplementary Fig. 4. 1a-FAP complex reversibility depends on the heavy chain scFvs FAP clone dH6.2

Cells that were not fed with any azido metabolites were transfected with either dH6.2-GFP-KDEL or light chain scFvs FAP variant dK-GFP-KDEL and stained with 500 nM **1a**. dH6.2 was shown to have reversible binding to MG[21,72], while dK features nanomolar affinity[21,72] and is thus irreversibly bound under experimental conditions. **a**, Cells imaged while in staining solution show co-localization of sensor (GFP) and fluorogen (**1a**) signal for both constructs. Scale = 10 µm. **b**, Cells imaged after washing 3x with DMEM show only fluorogen signal for the dK construct (top), as FAP-bound 1a is not washed out. Line profiles show the relative change in **1a** fluorescence intensity compared to GFP. Specific detection of SPAAC-conjugated fluorogens thus requires a lower affinity FAP like dH6.2. Scale = 25 µm.

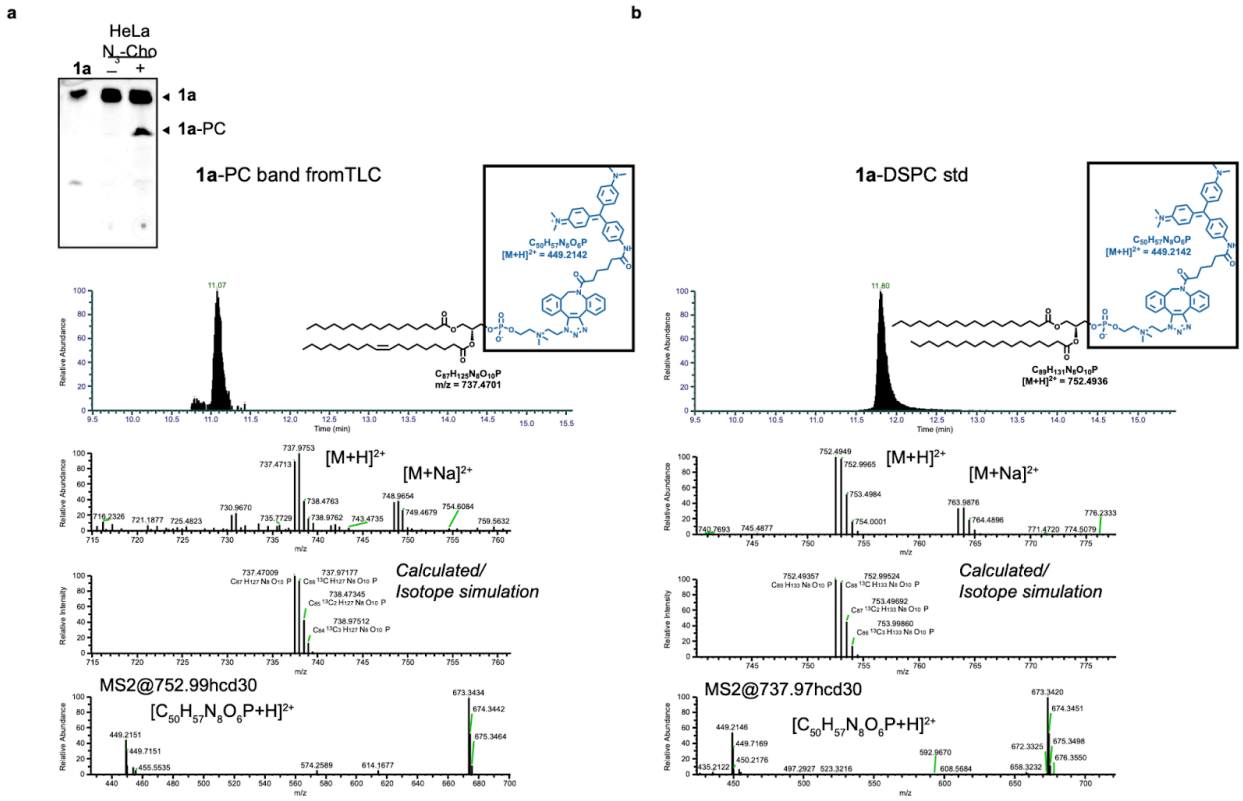

Supplementary Fig. 5. 1a-PC conjugates are formed in cells

a, HR-MS/MS analysis of **1a**-PC band from thin layer chromatography detecting $[M+H]^{2+}$=747.4713 and MS2 fragment 449.2146. Cells stained with **1a** were not washed prior to lipid extraction to highlight conversion of **1a** to **1a**-PC. **b**, Comparative HR-MS/MS analysis of the **1a**-DSPC standard previously synthesized by reaction of **1a** with N_3-DSPC detecting $[M+H]^{2+}$=752.4949 and MS2 fragment 449.2146.

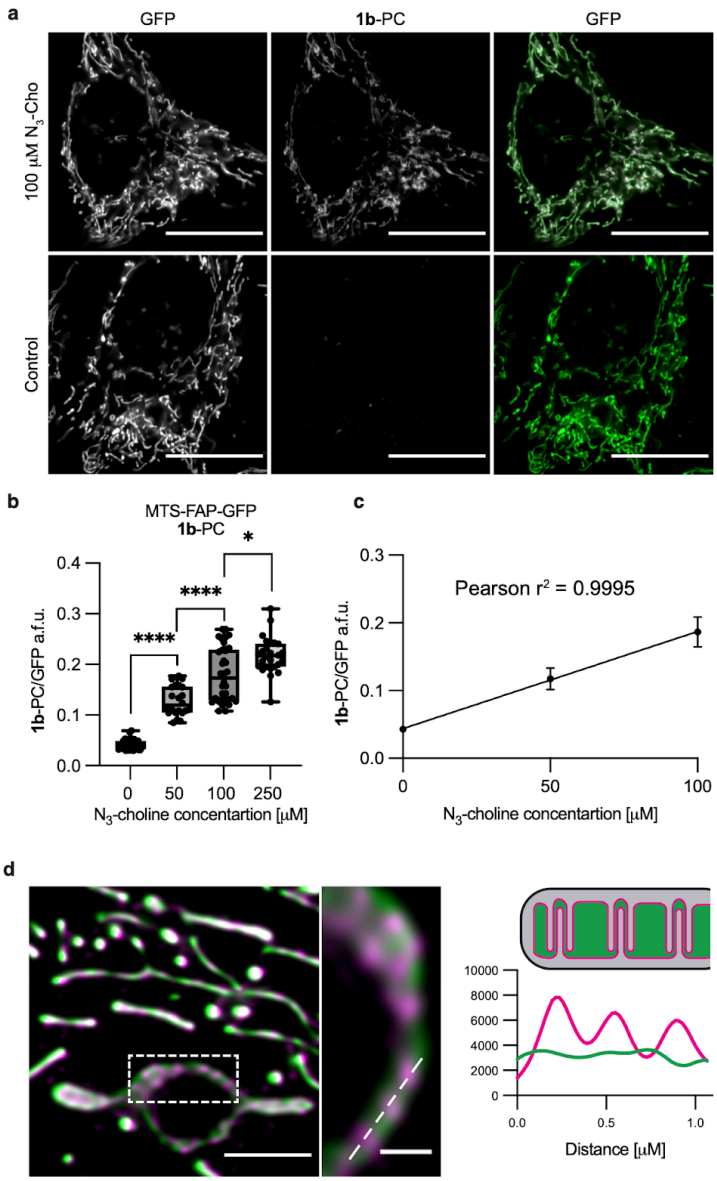

Supplementary Fig. 6. Linear quantification of 1b-PC in the mitochondrial matrix

a, HeLa cells stably expressing MTS-FAP-GFP were fed different concentrations of N_3-Cho for 24h and stained with 500 nM **1b**. Images show that fluorogen fluorescence (middle) is dependent on azido metabolic incorporation. Scale = 20 μm. **b**, Quantification of **1b**/GFP fluorescence in cells expressing MTS-FAP-GFP with increasing concentrations of N_3-Cho. **c**, Linear increase of **1b**/GFP fluorescence only up to 100 μM N_3-Cho. **d,** Super-resolution live cell imaging of **1b**-PC (magenta) in the mitochondrial matrix with Elyra 7 lattice SIM^2. The graph below indicates fluorescence intensity profiles of **1b**-PC (magenta) and GFP (green) along the white dashed line (inset). Scale = 2 μm and 0.5 μm, respectively.

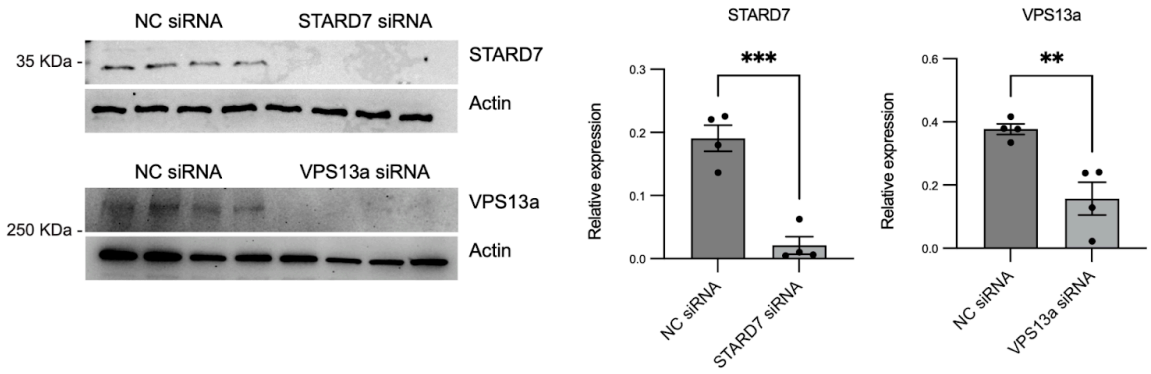

Supplementary Fig. 7. Silencing efficiency of STARD7 and VPS13a siRNAs

Cells were transfected with 25 pmol siRNA for 48 h and silencing efficiency was determined by western blotting. Antibodies for STARD7 and VPS13a were used at 1:1000 dilution, while actin was used as a loading control at 1:5000 dilution. Bar graphs reflect average expression relative to actin and error bars indicate SD; **, $p < 0.01$; ***, $p < 0.001$.

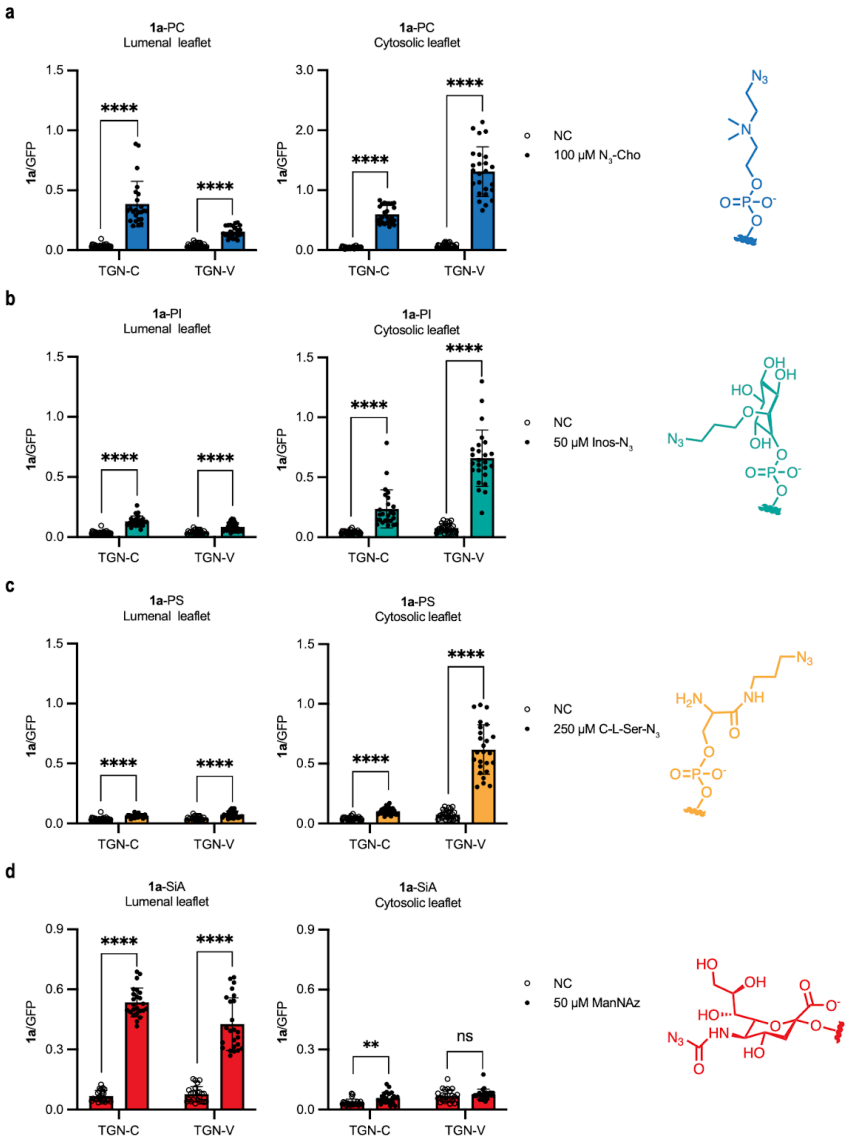

743

744 **Supplementary Fig. 8. FACES quantification of phospholipid asymmetry across the TGN**
745 Cells stably expressing doxycycline-inducible FAP-TGN38-GFP (luminal leaflet) or
746 GFP-TGN38-FAP (cytosolic leaflet) constructs were grown under 1 μg/mL doxycycline and fed
747 different azido metabolic labeling reagents for 24h prior to staining with 500 nM **1a**. **a,** cells fed
748 100 μM N_3-Cho. **b**, cells fed 50 μM Inos-N_3. **c**, cells fed 250 μM C-L-Ser-N_3. **d**, cells fed 50 μM
749 Ac_4ManNAz. LSM images were used for quantification. Structures of azido-containing lipid head
750 groups are provided. In all experiments *n* = 25 cells per condition; ****, $p < 0.001$, as determined
751 by Student's T-test.

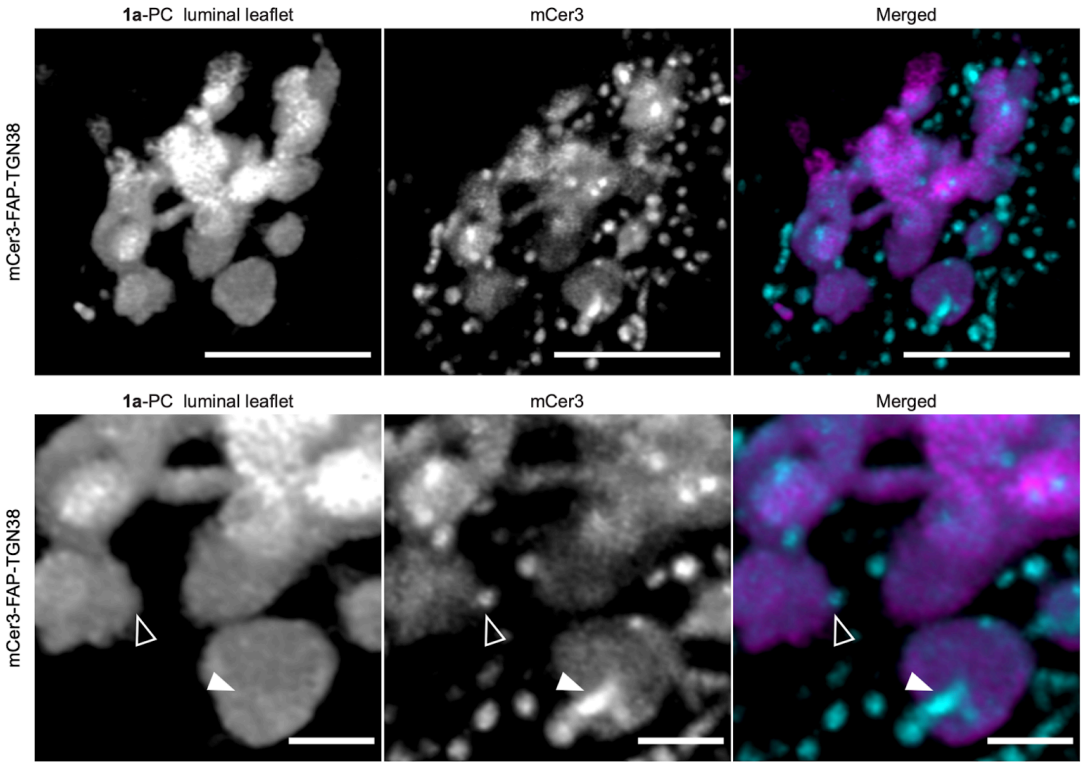

Supplementary Fig. 9. TGN vesicle formation is associated with a loss of luminal PC Golgi (top) and highlighted region (bottom) are shown from an individual cell were transfected with mCer3-FAP-TGN38, fed 100 μM N_3-Cho for 24h, and labeled with 500 nM **1a**. 3D rendering of Airyscan z-stacked images show a lack of **1a**-PC labeling on the luminal leaflet of vesicles (arrow, outline) and tubes (arrow, filled) connected to TGN cisternae. Airyscan images were acquired with 405 and 633 lasers for excitation and localization of mCer3 and **1a**-PC, respectively. Scale = 10 μm (top) and 2 μm (bottom).

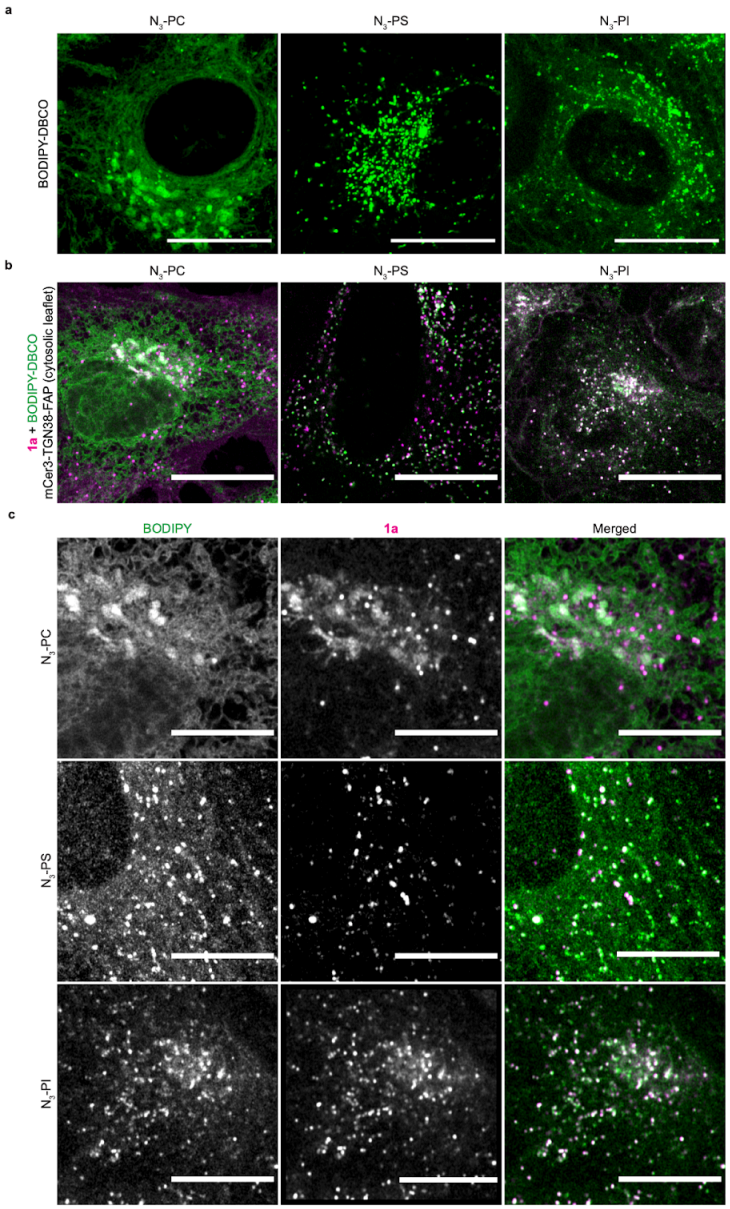

Supplementary Fig. 10. Multicolor imaging of global and targeted phospholipid pools Cells were metabolically labeled with 100 μM N_3-Cho, 250 μM C-L-Ser-N_3, or 50 μM Inos-N_3 for 24h prior to SPAAC conjugation. **a**, HeLa cells stained with 2 μM BODIPY-DBCO, which reacts with intracellular azido lipids. Images reflect maximal projection of Airyscan z-stacked images. Scale bars, 20 μm. **b**, Merged Airyscan images of HeLa cells stably expressing pTet:mCer3-TGN38-FAP double stained with equimolar (1 μM each) **1a**:BODIPY-DBCO. Scale

771 bars, 20 μm **c**, Higher magnification images show overlapping phospholipid distributions
772 between total lipids labeled with BODIPY and those labeled by **1a** and detected in the cytosolic
773 leaflet of the TGN. For experiments **b-c**, 488 and 633 nm laser lines were used for imaging to
774 avoid excitation of mCer3. Scale = 10 μm.
775

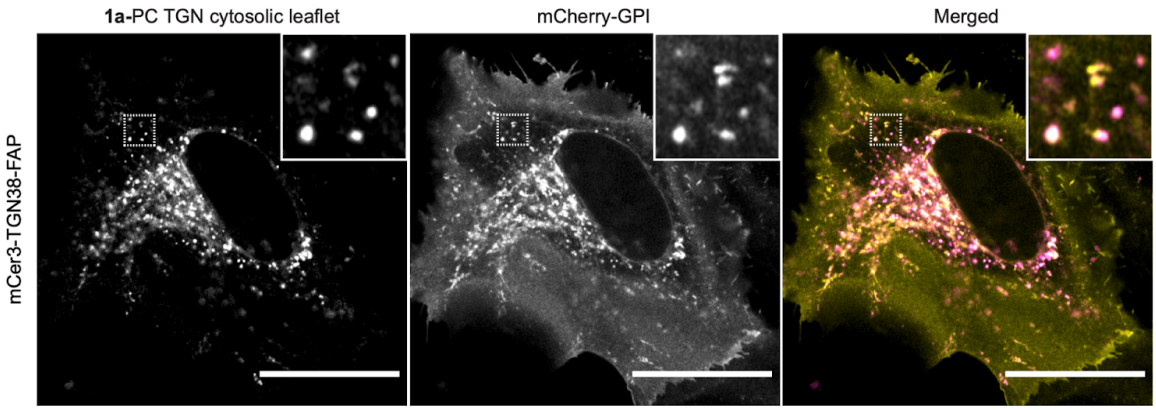

Supplementary Fig. 11. Secreted GPI-anchored proteins co-localize with cytoplasmic 1a-PC in TGN vesicles

Cells were cotransfected with mCherry-GPI and mCer3-TGN38-FAP constructs, fed 100 μM N_3-Cho for 24h, and labeled with 500 nM **1a.** Airyscan images were acquired using only 561 and 633 lasers for excitation of m-Cherry-GPI and **1a**-PC, respectively. Maximal projection of z-stacked images show co-localization between mCherry-GPI cargo and cytosolic facing **1a**-PC in TGN cisternae and vesicles (inset). Scale = 25 μm.

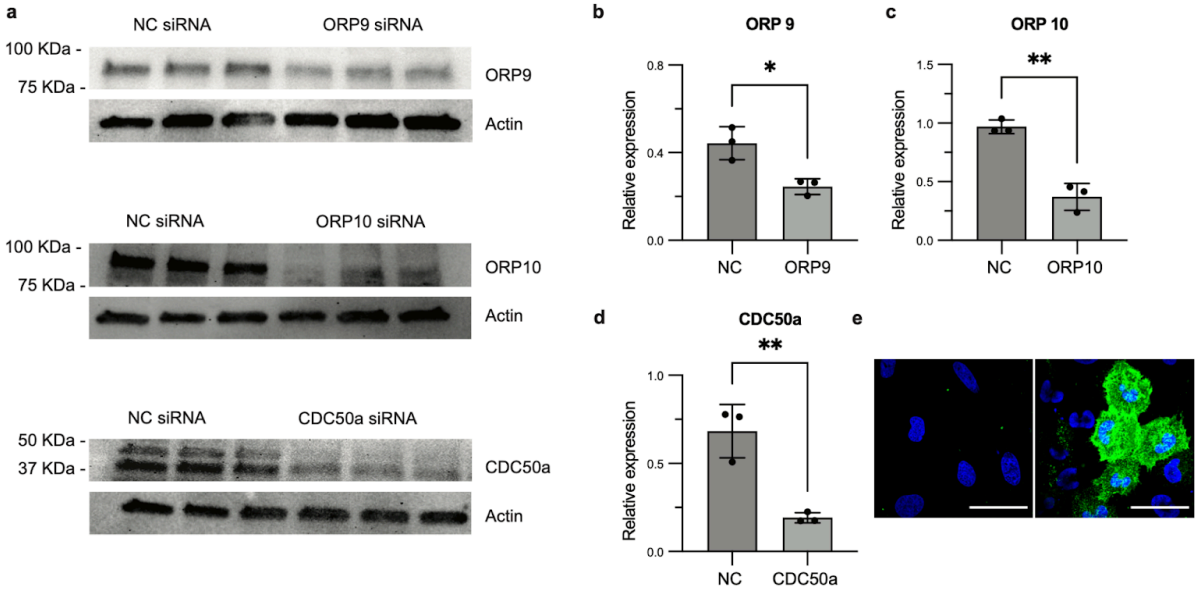

Supplementary Fig. 12. Silencing efficiency of ORP9, ORP10, and CDC50a siRNAs

Cells were transfected with siRNA for 48 h prior to analysis. **a**, Western blot analysis of ORP9, ORP10, and CDC50a from silencing experiments. Antibodies for target genes were used at 1:1000 and actin was used as a loading control (1:5000). **b**-**d**, Average band intensities normalized to actin (n = 3); *, $p < 0.05$; **, $p < 0.01$. **e**, Annexin V staining (green) of NC siRNA transfected cells (left) or CDC50a transfected cells (right). Nuclei were counterstained with Hoescht. Scale = 50 μm.

798

799 **Supplementary Movie 1: Mobility of TGN vesicles containing cytosolic PC and luminal SM**

800 Airyscan time-lapse of Golgi from the cell shown in Fig. 4d expressing GFP-EqtSM (cyan) and
801 mCer3-TGN38-FAP detecting **1a**-PC detection in the cytoplasmic leaflet (magenta). Images
802 reflect maximal intensity values from z-stacked images spanning 1.5 µm. Scale = 10 µm.

803 https://drive.google.com/file/d/1uWdM-LxW6N6hfmS_1oAvt9gelVmVm2tq/view?usp=sharing

804

805 **Supplementary Movie 2: Mobility of TGN vesicles containing cytosolic PC and protein**
806 **cargoes**

807 Airyscan time-lapse of Golgi from the cell shown in Supplementary Fig. 10 expressing
808 mCherry-SBP-GPI (yellow) and mCer3-TGN38-FAP detecting **1a**-PC detection in the
809 cytoplasmic leaflet (magenta). Scale = 20 µm.

810 https://drive.google.com/file/d/1S8RHj0p4P12DSThlM9wqXF7-yQTGs2qc/view?usp=sharing

811

Supplementary Text: Synthesis of the Malachite Green Probes

Commercially available 4-nitrobenzaldehyde, *N*,*N*-dimethylaniline, niobium(V) chloride ($NbCl_5$), 10% Pd/C, O-(7-azabenzotriazol-1-yl)- 1,1,3,3-tetramethyluronium hexafluoro-phosphate (HATU), *N*,*N*-diisopropylethylamine (DIEA), tetrachloro-*p*-benzoquinone, and glacial acetic acid (AcOH) were obtained from Sigma-Aldrich. DBCO-C_6-CO_2H, azido-PEG_2-CH_2CO_2H, and DBCO-PEG_2-CO_2H were obtained from BroadPharm. Deuterated chloroform ($CDCl_3$) was obtained from Cambridge Isotope Laboratories. All reagents obtained from commercial suppliers were used without further purification unless otherwise noted. Analytical thin-layer chromatography was performed on E. Merck silica gel 60 F_{254} plates. Silica gel flash chromatography was performed using E. Merck silica gel (type 60SDS, 230-400 mesh). Solvent mixtures for chromatography are reported as v/v ratios. HPLC analysis was carried out on an Eclipse Plus C8 analytical column with *Phase A*/*Phase B* gradients [*Phase A*: H_2O with 0.1% formic acid; *Phase B*: MeOH with 0.1% formic acid]. HPLC purification was carried out on Zorbax SB-C18 semipreparative column with *Phase A*/*Phase B* gradients [*Phase A*: H_2O with 0.1% formic acid; *Phase B*: MeOH with 0.1% formic acid]. Proton nuclear magnetic resonance (^{1}H NMR) spectra were recorded on a Jeol ECZL 400 MHz spectrometer, and were referenced relative to residual proton resonances in $CDCl_3$ (at d 7.26 ppm) or CD_3OD (at d 4.87 or 3.31 ppm). ^{1}H NMR splitting patterns are assigned as singlet (s), doublet (d), triplet (t), quartet (q) or pentuplet (p). All first-order splitting patterns were designated on the basis of the appearance of the multiplet. Splitting patterns that could not be readily interpreted are designated as multiplet (m) or broad (br). Carbon nuclear magnetic resonance (^{13}C NMR) spectra were recorded on a Jeol ECZL 400 MHz spectrometer, and were referenced relative to residual proton resonances in $CDCl_3$ (at d 77.16 ppm) or CD_3OD (at d 49.15 ppm). Electrospray Ionization-Time of Flight (ESI-TOF) spectra were obtained on an Agilent 6230 TOF-MS.

838 4,4'-((4-nitrophenyl)methylene)bis(*N*,*N*-dimethylaniline) [O_2N-Malachite Green *(Leuco form)*][78,79]**.**
839 A mixture of 4-nitrobenzaldehyde (0.755 g, 5.0 mmol), *N*,*N*-dimethylaniline (1.90 mL, 15.0
840 mmol), and $NbCl_5$ (0.135 g, 0.5 mmol) was heated at 130 ºC for 2 h under Ar. Several color
841 changes were observed, from yellow to orange, and finally purple. Afterwards, the reaction
842 mixture was cooled to room temperature and diluted in EtOAc (20 mL) and H_2O (20 mL). The
843 aqueous layer was then extracted with EtOAc (3 × 10 mL), and the combined organic layers
844 were dried over anhydrous $MgSO_4$ and concentrated *in vacuo*. The crude was absorbed over
845 SiO_2, and then purified by flash column chromatography (10-20% EtOAc in hexanes), affording
846 1.486 g of O_2N-Malachite Green *(Leuco form)* as an orange solid [79%, Rf = 0.42 (20% EtOAc
847 in hexanes)]. ^{1}H NMR ($CDCl_3$, 400.13 MHz, d): 8.12 (d, *J* = 8.7 Hz, 2H, 2 × CH), 7.30 (d, *J* = 8.7
848 Hz, 2H, 2 × CH), 6.96 (d, *J* = 8.7 Hz, 4H, 4 × CH), 6.69 (d, *J* = 8.2 Hz, 4H, 4 × CH), 5.47 (s, 1H,
849 1 × CH), 2.94 (s, 12H, 4 × CH_3). ^{13}C NMR ($CDCl_3$, 100.61 MHz, d): 153.3, 149.2, 146.3, 131.1,
850 130.2, 130.0, 123.6, 112.8, 55.0, 40.8. MS (ESI-TOF) [m/z (%)]: 376 ($[MH]^+$, 34), 188 ($[MH]^{2+}$,
851 100).
852
853 4,4'-((4-aminophenyl)methylene)bis(*N*,*N*-dimethylaniline) [H_2N-Malachite Green *(Leuco form)*]. A
854 suspension of 4,4'-((4-nitrophenyl)methylene)bis(*N*,*N*-dimethylaniline) [O_2N-Malachite Green
855 (*Leuco form*)), 150.0 mg, 0.40 mmol] and 10% Pd/C (42.6 mg) in absolute EtOH (8 mL) was
856 stirred for 2 h under H_2. Then, the mixture was filtered through a pad of celite, washing with
857 EtOH (3 × 2 mL). Afterwards, the filtrate was concentrated *in vacuo*, affording 137.2 mg of
858 H_2N-Malachite Green (*Leuco form*) as a white solid [99%, Rf = 0.42 (20% EtOAc in hexanes)].
859 The product was used directly without any further purification. ^{1}H NMR ($CDCl_3$, 400.13 MHz, d):
860 7.00 (d, *J* = 8.7 Hz, 4H, 4 × CH), 6.92 (d, *J* = 8.3 Hz, 2H, 2 × CH), 6.69 (d, *J* = 8.7 Hz, 4H, 4 ×
861 CH), 6.61 (d, *J* = 8.3 Hz, 2H, 2 × CH), 5.29 (s, 1H, 1 × CH), 3.86 (br s, 2H, 1 × NH_2), 2.92 (s,
862 12H, 4 × CH_3). ^{13}C NMR ($CDCl_3$, 100.61 MHz, d): 148.8, 144.2, 135.8, 133.8, 130.2, 130.0,
863 115.2, 112.8, 54.2, 41.0. MS (ESI-TOF) [m/z (%)]: 346 ($[MH]^+$, 11), 173 ($[MH]^{2+}$, 100).

DBCO-C_6-Malachite Green (*Leuco form*). A solution of DBCO-C_6-CO_2H (19.3 µL, 57.9 mmol) in 100 µL of CH_2Cl_2 was stirred at 0 ºC for 10 min, and then HATU (24.2 mg, 63.7 mmol) and DIEA (40.4 µL, 231.6 µmol) were successively added. After 10 min stirring at 0 ºC, a H_2N-Malachite Green *(Leuco form)* (20.0 mg, 57.9 mmol) solution in 100 µL of CH_2Cl_2 containing DIEA (20.2 µL, 115.8 µmol) was added. After 1 h stirring at rt, the solvent was removed under reduced pressure to give a blue oil. The corresponding residue was dissolved in MeOH (400 µL), filtered using a 0.2 µm syringe-driven filter, and the crude solution was purified by HPLC, affording 29.2 mg of DBCO-C_6-Malachite Green *(Leuco form)* as a blue oil [72%, t_R = 10.8 min (Zorbax SB-C18 semipreparative column, 50% *Phase A* in *Phase B*, 1 min, then 50-5% *Phase A* in *Phase B*, 5 min, and then 5% *Phase A* in *Phase B*, 10 min)]. ^{1}H NMR ($CDCl_3$, 400.13 MHz, d): 7.78 (s, 1H, 1 × NH), 7.72-7.64 (m, 1H, 1 × CH), 7.50-7.28 (m, 7H, 7 × CH), 7.25-7.18 (m, 4H, 4 × CH), 7.08-6.94 (m, 6H, 6 × CH), 6.93-6.72 (m, 2H, 2 × CH), 5.38 (s, 1H, 1 × CH), 5.17 (d, J = 13.8 Hz, 1H, 0.5 × CH_2), 3.69 (d, J = 13.8 Hz, 1H, 0.5 × CH_2), 2.96 (s, 12H, 4 × CH_3), 2.29 (dt, J_1 = 16.0 Hz, J_2 = 6.0 Hz, 1H, 0.5 × CH_2), 2.10 (dt, J_1 = 17.1 Hz, J_2 = 6.8 Hz, 1H, 0.5 × CH_2), 2.02-1.81 (m, 2H, 1 × CH_2), 1.62-1.40 (m, 3H, 1.5 × CH_2), 1.39-1.21 (m, 1H, 0.5 × CH_2). ^{13}C NMR ($CDCl_3$, 100.61 MHz, d): 173.8, 171.2, 151.7, 148.0, 132.5, 130.3, 129.8, 129.1, 128.6, 128.5, 128.4, 128.0, 127.3, 125.6, 123.1, 122.6, 119.9, 115.1, 108.0, 55.6, 54.7, 44.0, 36.8, 34.6, 25.1, 24.0. MS (ESI-TOF) [m/z (%)]: 661 ($[MHI]^+$, 5), 331 ($[MH]^{2+}$, 100).

DBCO-C_6-Malachite Green *(Chromatic form)* (**1a**). To a blue solution of DBCO-C_6-Malachite Green *(Leuco form)* (4.0 mg, 6.1 µmol) and tetrachloro-*p*-benzoquinone (1.8 mg, 7.3 µmol) in $CHCl_3$ (226 µL), glacial acetic acid (4.5 µL, 0.45 µmol) was added. The solution was stirred at 35 ºC for 2 h. Afterwards, the volatiles were removed under reduced pressure, obtaining a dark green residue. The crude was absorbed over SiO_2, and then purified by flash column chromatography (0-7% MeOH in CH_2Cl_2), affording 3.8 mg of DBCO-C_6-Malachite Green

890 *(Chromatic form)* as a dark green solid [90%, Rf = 0.57 (10% MeOH in CH_2Cl_2)]. ^{1}H NMR
891 (CD_3OD, 400.13 MHz, d): 7.91-7.76 (m, 4H, 4 × CH), 7.71-7.64 (m, 1H, 1 × NH), 7.57-7.47 (m,
892 2H, 2 × CH), 7.44 (d, *J* = 9.0 Hz, 4H, 4 × CH), 7.37 (d, *J* = 8.7 Hz, 2H, 2 × CH), 7.33-7.19 (m,
893 4H, 4 × CH), 7.06 (d, *J* = 9.4 Hz, 4H, 4 × CH), 4.93-4.91 (m, 2H, 1 × CH_2), 3.33 (s, 12H, 4 ×
894 CH_3), 2.52-2.45 (m, 2H, 1 × CH_2), 2.44-2.34 (m, 2H, 1 × CH_2), 1.83-1.65 (m, 4H, 2 × CH_2). ^{13}C
895 NMR (CD_3OD, 100.61 MHz, d): 178.9, 174.7, 158.4, 145.6, 141.9, 137.7, 135.8, 135.6, 134.2,
896 133.5, 130.8, 130.4, 130.0, 129.7, 129.2, 128.9, 128.8, 128.3, 126.5, 125.6, 124.3, 123.1, 120.7,
897 120.2, 114.8, 114.5, 114.2, 40.9, 37.7, 34.4, 33.1, 30.8, 26.0, 25.5. MS (ESI-TOF) [m/z (%)]: 660
898 ($[MH -Cl]^+$, 51), 659 ($[M -Cl]^+$, 100), 330 ($[MH -Cl]^{2+}$, 53).
899
900 <u>DBCO-PEG$_2$-Malachite Green *(Leuco form)*.</u> A solution of DBCO-PEG$_2$-CO_2H (13.4 mg, 28.9
901 mmol) in 200 µL of CH_2Cl_2/DMF (1:1) was stirred at 0 ºC for 10 min, and then HATU (12.1 mg,
902 31.8 mmol) and DIEA (20.2 µL, 115.8 µmol) were successively added. After 10 min stirring at 0
903 ºC, a H_2N-Malachite Green *(Leuco form)* (10.0 mg, 28.9 mmol) solution in 200 µL of
904 CH_2Cl_2/DMF (1:1) containing DIEA (10.1 µL, 57.9 µmol) was added. After 1 h stirring at rt, the
905 solvent was removed under reduced pressure to give a blue oil. The corresponding residue was
906 dissolved in MeOH (200 µL), filtered using a 0.2 µm syringe-driven filter, and the crude solution
907 was purified by HPLC, affording 13.2 mg of DBCO-PEG$_2$-Malachite Green *(Leuco form)* as a
908 blue oil [55%, t_R = 50.9 min (Zorbax SB-C18 semipreparative column, 95% *Phase A* in *Phase B*,
909 1 min, then 95-50% *Phase A* in *Phase B*, 30 min, and then 50-0% *Phase A* in *Phase B*, 22
910 min)]. ^{1}H NMR ($CDCl_3$, 400.13 MHz, d): 8.76 (s, 1H, 1 × NH), 7.60-7.54 (m, 1H, 1 × CH),
911 7.53-7.46 (m, 1H, 1 × CH), 7.46-7.34 (m, 6H, 6 × CH), 7.25-7.17 (m, 4H, 4 × CH), 7.09-6.96 (m,
912 6H, 6 × CH), 6.95-6.72 (m, 2H, 2 × CH), 6.28 (t, *J* = 5.6 Hz, 1H, 1 × NH), 5.36 (s, 1H, 1 × CH),
913 5.09 (d, *J* = 13.9 Hz, 1H, 0.5 × CH_2), 3.87-3.71 (m, 2H, 1 × CH_2), 3.69-3.56 (m, 5H, 2.5 × CH_2),
914 3.45 (t, *J* = 5.4 Hz, 2H, 1 × CH_2), 3.34-3.18 (m, 2H, 1 × CH_2), 2.95 (s, 12H, 4 × CH_3), 2.87-2.75
915 (m, 1H, 0.5 × CH_2), 2.53-2.41 (m, 2H, 1 × CH_2), 2.39-2.26 (m, 1H, 0.5 × CH_2), 2.17-2.02 (m, 1H,

0.5 × CH_2), 1.98-1.83 (m, 1H, 0.5 × CH_2). ^{13}C NMR ($CDCl_3$, 100.61 MHz, d): 172.7, 172.1, 169.9, 151.3, 148.1, 132.3, 130.3, 129.8, 129.5, 128.9, 128.4, 128.2, 127.9, 127.2, 125.6, 123.2, 122.6, 119.9, 114.8, 108.0, 70.7, 69.9, 69.8, 67.4, 55.8, 54.8, 39.1, 38.0, 31.5, 30.3. MS (ESI-TOF) [m/z (%)]: 793 ($[MH]^+$, 4), 397 ($[MH]^{2+}$, 100).

DBCO-PEG$_2$-Malachite Green *(Chromatic form)* (**1b**). To a blue solution of DBCO-PEG$_2$-Malachite Green *(Leuco form)* (5.0 mg, 6.3 μmol) and tetrachloro-*p*-benzoquinone (1.9 mg, 7.6 μmol) in $CHCl_3$ (235 μL), glacial acetic acid (4.7 μL, 0.47 μmol) was added. The solution was stirred at 35 ºC for 2 h. Afterwards, the volatiles were removed under reduced pressure, obtaining a dark green residue. The crude was absorbed over SiO_2, and then purified by flash column chromatography (0-10% MeOH in CH_2Cl_2), affording 4.8 mg of N_3-PEG$_2$-Malachite Green *(Chromatic form)* as a dark green solid [92%, Rf = 0.44 (10% MeOH in CH_2Cl_2)]. ^1H NMR ($CDCl_3$, 400.13 MHz, d): 11.33 (s, 1H, 1 × NH), 8.20 (d, *J* = 8.4 Hz, 2H, 2 × CH), 7.85-7.69 (m, 1H, 1 × NH), 7.63 (d, *J* = 7.3 Hz, 1H, 1 × CH), 7.58 (d, *J* = 7.6 Hz, 1H, 1 × CH), 7.42-7.27 (m, 9H, 9 × CH), 7.25-7.17 (m, 3H, 3 × CH), 6.86 (d, *J* = 8.5 Hz, 4H, 4 × CH), 5.13 (d, *J* = 13.9 Hz, 1H, 0.5 × CH_2), 3.91 (t, *J* = 5.9 Hz, 2H, 1 × CH_2), 3.76-3.57 (m, 5H, 2.5 × CH_2), 3.56-3.45 (m, 2H, 1 × CH_2), 3.31 (s, 12H, 4 × CH_3), 2.94 (t, *J* = 5.9 Hz, 2H, 1 × CH_2), 2.87-2.75 (m, 1H, 0.5 × CH_2), 2.68-2.53 (m, 1H, 0.5 × CH_2), 2.46-2.26 (m, 4H, 2 × CH_2). ^{13}C NMR ($CDCl_3$, 100.61 MHz, d): 175.7, 174.4, 172.4, 156.5, 146.3, 141.1, 137.4, 134.2, 133.4, 133.3, 132.3, 129.3, 127.7, 127.6, 125.8, 124.9, 124.4, 122-1, 121.9, 120.0, 119.9, 117.3, 113.6, 133.5, 98.1, 98.0, 70.4, 70.3, 68.9, 67.3, 47.0, 41.2, 40.4, 38.0, 32.1, 29.9, 29.5, 22.9*, 14.3*. MS (ESI-TOF) [m/z (%)]: 791 ($[MH -Cl]^+$, 3), 396 ($[MH -Cl]^{2+}$, 100). *Artifact.

^{1}H (left) and ^{13}C NMR (right) spectra of synthesized compounds and key intermediates

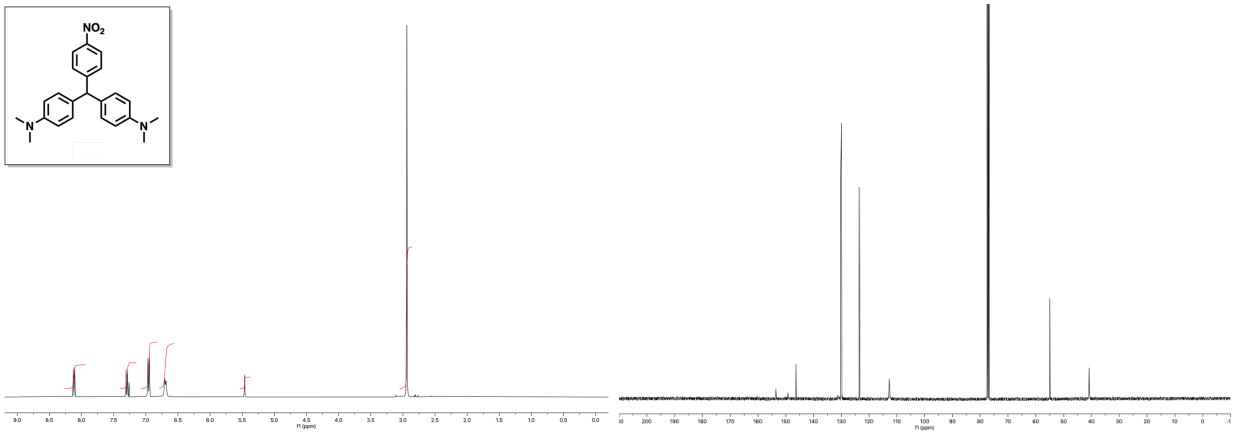

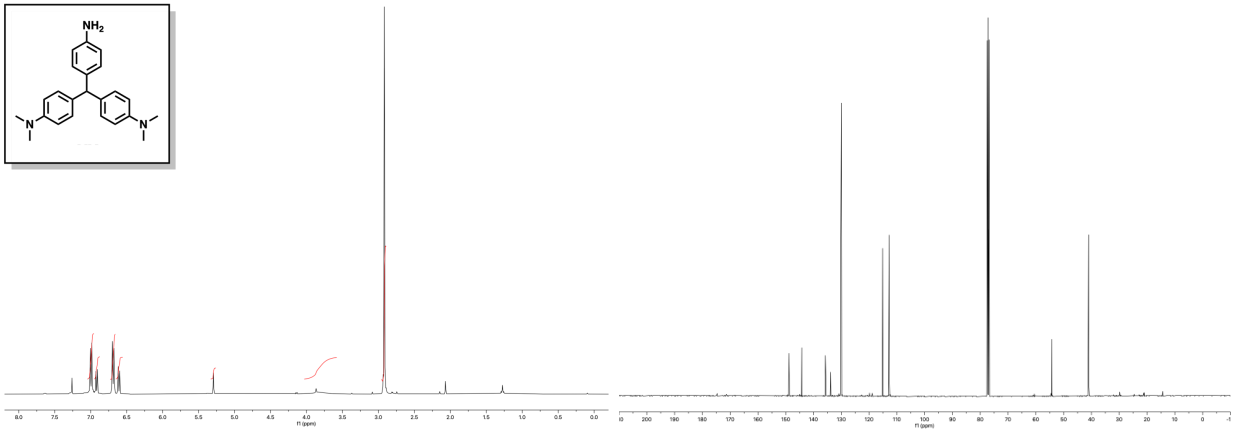

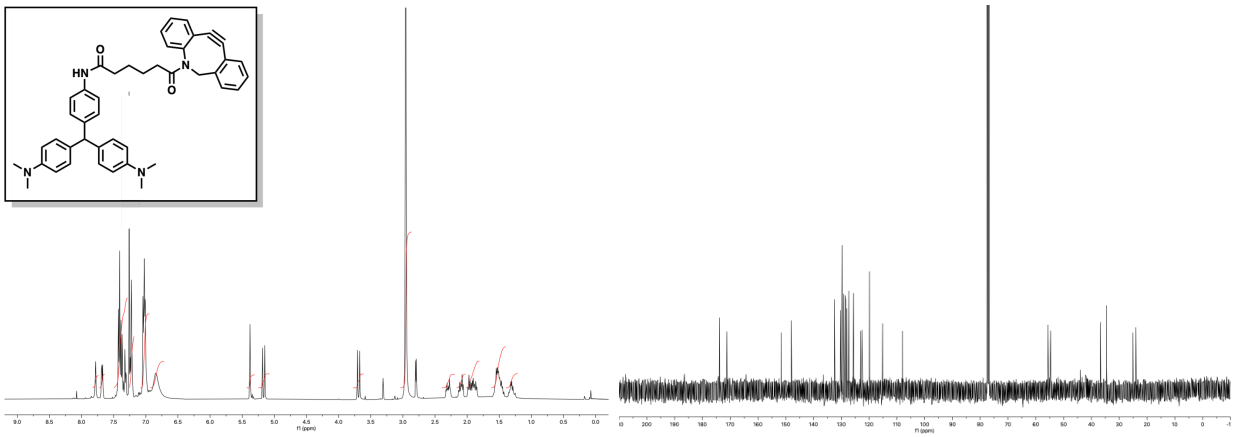

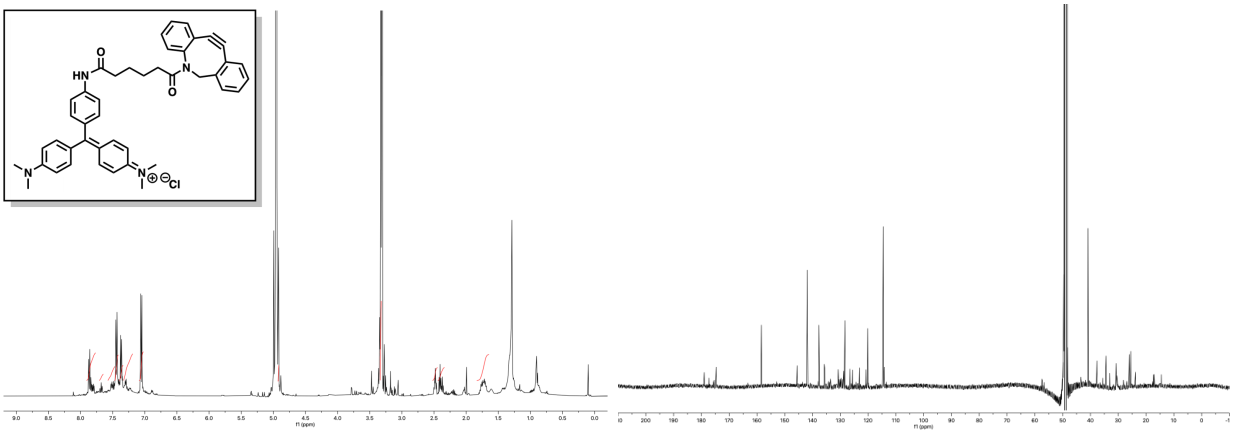

944

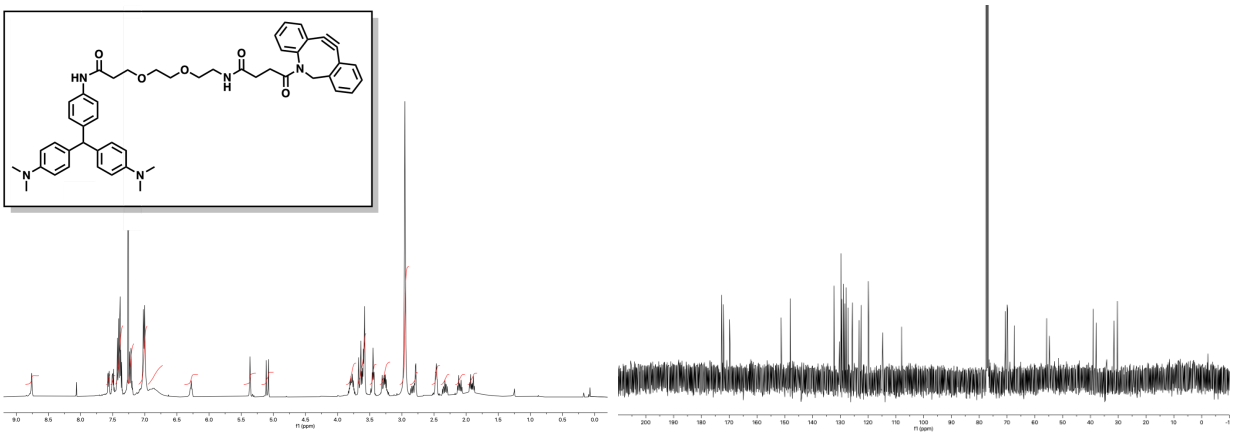

945

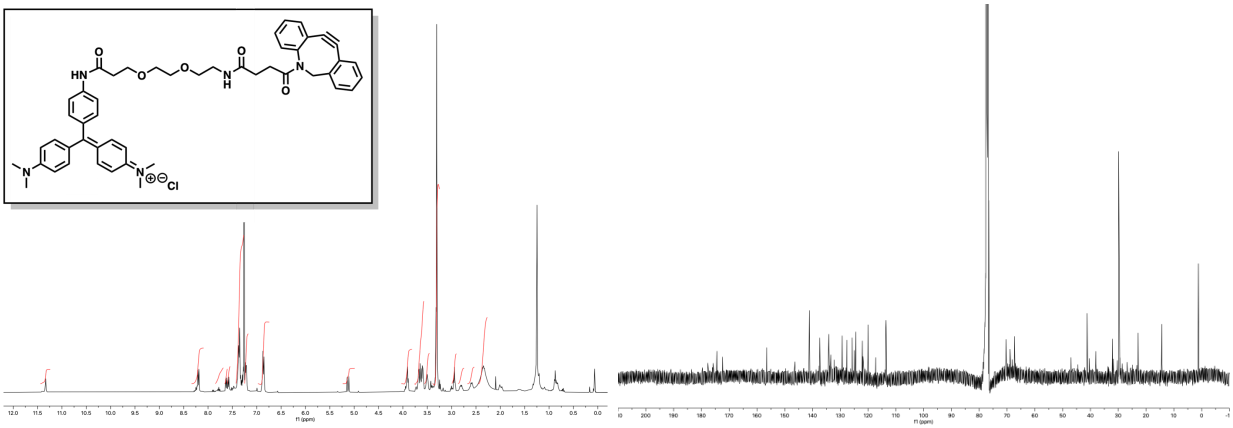

946

947

References

1. van Meer, G., Voelker, D. R. & Feigenson, G. W. Membrane lipids: where they are and how they behave. *Nat. Rev. Mol. Cell Biol.* **9**, 112–124 (2008).
2. Levental, I. & Lyman, E. Regulation of membrane protein structure and function by their lipid nano-environment. *Nat. Rev. Mol. Cell Biol.* **24**, 107–122 (2023).
3. Lorent, J. H. *et al.* Plasma membranes are asymmetric in lipid unsaturation, packing and protein shape. *Nat. Chem. Biol.* **16**, 644–652 (2020).
4. Khaddaj, R. & Kukulski, W. Piecing together the structural organisation of lipid exchange at membrane contact sites. *Curr. Opin. Cell Biol.* **83**, 102212 (2023).
5. Voeltz, G. K., Sawyer, E. M., Hajnóczky, G. & Prinz, W. A. Making the connection: How membrane contact sites have changed our view of organelle biology. *Cell* **187**, 257–270 (2024).
6. Wong, L. H., Gatta, A. T. & Levine, T. P. Lipid transfer proteins: the lipid commute via shuttles, bridges and tubes. *Nat. Rev. Mol. Cell Biol.* **20**, 85–101 (2019).
7. Lipp, N.-F., Ikhlef, S., Milanini, J. & Drin, G. Lipid Exchangers: Cellular Functions and Mechanistic Links With Phosphoinositide Metabolism. *Front Cell Dev Biol* **8**, 663 (2020).
8. Rothman, J. E. & Lenard, J. Membrane asymmetry. *Science* **195**, 743–753 (1977).
9. Verkleij, A. J. *et al.* The asymmetric distribution of phospholipids in the human red cell membrane. A combined study using phospholipases and freeze-etch electron microscopy. *Biochim. Biophys. Acta* **323**, 178–193 (1973).
10. Jao, C. Y., Roth, M., Welti, R. & Salic, A. Metabolic labeling and direct imaging of choline phospholipids in vivo. *Proc. Natl. Acad. Sci. U. S. A.* **106**, 15332–15337 (2009).
11. Ancajas, C. F. *et al.* Cellular labeling of phosphatidylserine using clickable Serine probes. *ACS Chem. Biol.* **18**, 377–384 (2023).
12. Ricks, T. J. *et al.* Labeling of Phosphatidylinositol Lipid Products in Cells through Metabolic

974 Engineering by Using a Clickable myo-Inositol Probe. *Chembiochem* **20**, 172–180 (2019).
975 13. Bumpus, T. W. & Baskin, J. M. A Chemoenzymatic Strategy for Imaging Cellular
976 Phosphatidic Acid Synthesis. *Angew. Chem. Int. Ed Engl.* **55**, 13155–13158 (2016).
977 14. Bussink, A. P. *et al.* N-azidoacetylmannosamine-mediated chemical tagging of
978 gangliosides. *J. Lipid Res.* **48**, 1417–1421 (2007).
979 15. Tamura, T. *et al.* Organelle membrane-specific chemical labeling and dynamic imaging in
980 living cells. *Nat. Chem. Biol.* **16**, 1361–1367 (2020).
981 16. Maekawa, M., Yang, Y. & Fairn, G. D. Perfringolysin O Theta Toxin as a Tool to Monitor the
982 Distribution and Inhomogeneity of Cholesterol in Cellular Membranes. *Toxins* **8**, (2016).
983 17. Deng, Y., Rivera-Molina, F. E., Toomre, D. K. & Burd, C. G. Sphingomyelin is sorted at the
984 trans Golgi network into a distinct class of secretory vesicle. *Proc. Natl. Acad. Sci. U. S. A.*
985 **113**, 6677–6682 (2016).
986 18. Gallo, E. Fluorogen-Activating Proteins: Next-Generation Fluorescence Probes for
987 Biological Research. *Bioconjug. Chem.* **31**, 16–27 (2020).
988 19. Kozma, E. & Kele, P. Fluorogenic probes for super-resolution microscopy. *Org. Biomol.*
989 *Chem.* **17**, 215–233 (2019).
990 20. Bottone, S. *et al.* A fluorogenic chemically induced dimerization technology for controlling,
991 imaging and sensing protein proximity. *Nat. Methods* **20**, 1553–1562 (2023).
992 21. Yan, Q. *et al.* Localization microscopy using noncovalent fluorogen activation by genetically
993 encoded fluorogen-activating proteins. *Chemphyschem* **15**, 687–695 (2014).
994 22. Horibata, Y. & Sugimoto, H. Differential contributions of choline phosphotransferases CPT1
995 and CEPT1 to the biosynthesis of choline phospholipids. *J. Lipid Res.* **62**, 100100 (2021).
996 23. Ng, M. N. P., Kitos, T. E. & Cornell, R. B. Contribution of lipid second messengers to the
997 regulation of phosphatidylcholine synthesis during cell cycle re-entry. *Biochim. Biophys.*
998 *Acta* **1686**, 85–99 (2004).
999 24. Adibhatla, R. M., Hatcher, J. F. & Gusain, A. Tricyclodecan-9-yl-xanthogenate (D609)

1000 mechanism of actions: a mini-review of literature. *Neurochem. Res.* **37**, 671–679 (2012).
1001 25. Larsen, E. C., Hatcher, J. F. & Adibhatla, R. M. Effect of tricyclodecan-9-yl potassium
1002 xanthate (D609) on phospholipid metabolism and cell death during oxygen-glucose
1003 deprivation in PC12 cells. *Neuroscience* **146**, 946–961 (2007).
1004 26. Stephan, T., Roesch, A., Riedel, D. & Jakobs, S. Live-cell STED nanoscopy of
1005 mitochondrial cristae. *Sci. Rep.* **9**, 12419 (2019).
1006 27. John Peter, A. T., Petrungaro, C., Peter, M. & Kornmann, B. METALIC reveals
1007 interorganelle lipid flux in live cells by enzymatic mass tagging. *Nat. Cell Biol.* **24**, 996–1004
1008 (2022).
1009 28. Kumar, N. *et al.* VPS13A and VPS13C are lipid transport proteins differentially localized at
1010 ER contact sites. *J. Cell Biol.* **217**, 3625–3639 (2018).
1011 29. Horibata, Y. *et al.* StarD7 Protein Deficiency Adversely Affects the Phosphatidylcholine
1012 Composition, Respiratory Activity, and Cristae Structure of Mitochondria. *J. Biol. Chem.*
1013 **291**, 24880–24891 (2016).
1014 30. Horibata, Y. & Sugimoto, H. StarD7 mediates the intracellular trafficking of
1015 phosphatidylcholine to mitochondria. *J. Biol. Chem.* **285**, 7358–7365 (2010).
1016 31. Horibata, Y. *et al.* Identification of the N-terminal transmembrane domain of StarD7 and its
1017 importance for mitochondrial outer membrane localization and phosphatidylcholine transfer.
1018 *Sci. Rep.* **7**, 8793 (2017).
1019 32. Bos, K., Wraight, C. & Stanley, K. K. TGN38 is maintained in the trans-Golgi network by a
1020 tyrosine-containing motif in the cytoplasmic domain. *EMBO J.* **12**, 2219–2228 (1993).
1021 33. Luzio, J. P. *et al.* Identification, sequencing and expression of an integral membrane protein
1022 of the trans-Golgi network (TGN38). *Biochem. J* **270**, 97–102 (1990).
1023 34. Iyoshi, S. *et al.* Asymmetrical distribution of choline phospholipids revealed by click
1024 chemistry and freeze-fracture electron microscopy. *ACS Chem. Biol.* **9**, 2217–2222 (2014).
1025 35. Cabukusta, B. *et al.* A lipid transfer protein knockout library reveals ORP9-ORP11 dimer

1026 mediating PS/PI(4)P exchange at the ER-trans Golgi contact site to promote sphingomyelin
1027 synthesis. *bioRxiv* 2023.06.02.543249 (2023) doi:10.1101/2023.06.02.543249.
1028 36. Phillips, S. E., Ile, K. E., Boukhelifa, M., Huijbregts, R. P. H. & Bankaitis, V. A. Specific and
1029 nonspecific membrane-binding determinants cooperate in targeting phosphatidylinositol
1030 transfer protein beta-isoform to the mammalian trans-Golgi network. *Mol. Biol. Cell* **17**,
1031 2498–2512 (2006).
1032 37. Fairn, G. D. *et al.* High-resolution mapping reveals topologically distinct cellular pools of
1033 phosphatidylserine. *J. Cell Biol.* **194**, 257–275 (2011).
1034 38. Saxon, E. & Bertozzi, C. R. Cell surface engineering by a modified Staudinger reaction.
1035 *Science* **287**, 2007–2010 (2000).
1036 39. Fleischer, B. Mechanism of glycosylation in the Golgi apparatus. *J. Histochem. Cytochem.*
1037 **31**, 1033–1040 (1983).
1038 40. Klemm, R. W. *et al.* Segregation of sphingolipids and sterols during formation of secretory
1039 vesicles at the trans-Golgi network. *J. Cell Biol.* **185**, 601–612 (2009).
1040 41. Doktorova, M. *et al.* Cell Membranes Sustain Phospholipid Imbalance Via Cholesterol
1041 Asymmetry. *bioRxiv* 2023.07.30.551157 (2023) doi:10.1101/2023.07.30.551157.
1042 42. Takar, M., Huang, Y. & Graham, T. R. The PQ-loop protein Any1 segregates Drs2 and Neo1
1043 functions required for viability and plasma membrane phospholipid asymmetry. *J. Lipid Res.*
1044 **60**, 1032–1042 (2019).
1045 43. Hankins, H. M., Sere, Y. Y., Diab, N. S., Menon, A. K. & Graham, T. R. Phosphatidylserine
1046 translocation at the yeast trans-Golgi network regulates protein sorting into exocytic
1047 vesicles. *Mol. Biol. Cell* **26**, 4674–4685 (2015).
1048 44. Takar, M., Wu, Y. & Graham, T. R. The essential Neo1 protein from budding yeast plays a
1049 role in establishing aminophospholipid asymmetry of the plasma membrane. *J. Biol. Chem.*
1050 **291**, 15727–15739 (2016).
1051 45. Chen, S. *et al.* Roles for the Drs2p-Cdc50p complex in protein transport and

1052 phosphatidylserine asymmetry of the yeast plasma membrane. *Traffic* **7**, 1503–1517
1053 (2006).
1054 46. Alder-Baerens, N., Lisman, Q., Luong, L., Pomorski, T. & Holthuis, J. C. M. Loss of P4
1055 ATPases Drs2p and Dnf3p disrupts aminophospholipid transport and asymmetry in yeast
1056 post-Golgi secretory vesicles. *Mol. Biol. Cell* **17**, 1632–1642 (2006).
1057 47. He, R. *et al.* ORP9 and ORP10 form a heterocomplex to transfer phosphatidylinositol
1058 4-phosphate at ER-TGN contact sites. *Cell. Mol. Life Sci.* **80**, 77 (2023).
1059 48. Kawasaki, A. *et al.* PI4P/PS countertransport by ORP10 at ER-endosome membrane
1060 contact sites regulates endosome fission. *J. Cell Biol.* **221**, (2022).
1061 49. Cabukusta, B. *et al.* A lipid transfer protein knockout library reveals ORP9-ORP11 dimer
1062 mediating PS/PI(4)P exchange at the ER-trans Golgi contact site to promote sphingomyelin
1063 synthesis. *eLife* (2023) doi:10.7554/elife.91345.1.
1064 50. Tanaka, Y. *et al.* The phospholipid flippase ATP9A is required for the recycling pathway
1065 from the endosomes to the plasma membrane. *Mol. Biol. Cell* **27**, 3883–3893 (2016).
1066 51. Takatsu, H. *et al.* Phospholipid Flippase Activities and Substrate Specificities of Human
1067 Type IV P-type ATPases Localized to the Plasma Membrane *. *J. Biol. Chem.* **289**,
1068 33543–33556 (2014).
1069 52. Best, J. T., Xu, P. & Graham, T. R. Phospholipid flippases in membrane remodeling and
1070 transport carrier biogenesis. *Curr. Opin. Cell Biol.* **59**, 8–15 (2019).
1071 53. Segawa, K., Kurata, S. & Nagata, S. The CDC50A extracellular domain is required for
1072 forming a functional complex with and chaperoning phospholipid flippases to the plasma
1073 membrane. *J. Biol. Chem.* **293**, 2172–2182 (2018).
1074 54. Coleman, J. A. & Molday, R. S. Critical role of the beta-subunit CDC50A in the stable
1075 expression, assembly, subcellular localization, and lipid transport activity of the P4-ATPase
1076 ATP8A2. *J. Biol. Chem.* **286**, 17205–17216 (2011).
1077 55. Boyce, M. *et al.* Metabolic cross-talk allows labeling of O-linked

1078 β-*N*-acetylglucosamine-modified proteins via the *N*-acetylgalactosamine salvage pathway.
1079 *Proceedings of the National Academy of Sciences* **108**, 3141–3146 (2011).
1080 56. Hang, H. C., Yu, C., Kato, D. L. & Bertozzi, C. R. A metabolic labeling approach toward
1081 proteomic analysis of mucin-type O-linked glycosylation. *Proc. Natl. Acad. Sci. U. S. A.* **100**,
1082 14846–14851 (2003).
1083 57. Ma, Z. & Vosseller, K. Cancer Metabolism and Elevated O-GlcNAc in Oncogenic Signaling*.
1084 *J. Biol. Chem.* **289**, 34457–34465 (2014).
1085 58. Tan, E. P. *et al.* Sustained O-GlcNAcylation reprograms mitochondrial function to regulate
1086 energy metabolism. *J. Biol. Chem.* **292**, 14940–14962 (2017).
1087 59. Zhu, Q. *et al.* *O*-GlcNAcylation promotes tumor immune evasion by inhibiting PD-L1
1088 lysosomal degradation. *Proceedings of the National Academy of Sciences* **120**,
1089 e2216796120 (2023).
1090 60. Pekkurnaz, G., Trinidad, J. C., Wang, X., Kong, D. & Schwarz, T. L. Glucose regulates
1091 mitochondrial motility via Milton modification by O-GlcNAc transferase. *Cell* **158**, 54–68
1092 (2014).
1093 61. Dupas, T. *et al.* An overview of tools to decipher O-GlcNAcylation from historical
1094 approaches to new insights. *Int. J. Biochem. Cell Biol.* **151**, 106289 (2022).
1095 62. Onodera, Y., Nam, J.-M. & Bissell, M. J. Increased sugar uptake promotes oncogenesis via
1096 EPAC/RAP1 and O-GlcNAc pathways. *J. Clin. Invest.* **124**, 367–384 (2014).
1097 63. Jóźwiak, P. *et al.* Mitochondrial O-GlcNAc Transferase Interacts with and Modifies Many
1098 Proteins and Its Up-Regulation Affects Mitochondrial Function and Cellular Energy
1099 Homeostasis. *Cancers* **13**, (2021).
1100 64. Ma, J. *et al.* O-GlcNAcomic Profiling Identifies Widespread O-Linked
1101 β-N-Acetylglucosamine Modification (O-GlcNAcylation) in Oxidative Phosphorylation
1102 System Regulating Cardiac Mitochondrial Function. *J. Biol. Chem.* **290**, 29141–29153
1103 (2015).

1104 65. Guzmán, L. E. *et al.* Bioorthogonal Metabolic Labeling of the Virulence Factor Phenolic
1105 Glycolipid in Mycobacteria. *ACS Chem. Biol.* (2024) doi:10.1021/acschembio.3c00724.
1106 66. Fantoni, N. Z., El-Sagheer, A. H. & Brown, T. A Hitchhiker's Guide to Click-Chemistry with
1107 Nucleic Acids. *Chem. Rev.* **121**, 7122–7154 (2021).
1108 67. Liang, D. *et al.* A real-time, click chemistry imaging approach reveals stimulus-specific
1109 subcellular locations of phospholipase D activity. *Proc. Natl. Acad. Sci. U. S. A.* **116**,
1110 15453–15462 (2019).
1111 68. Nguyen, S. S. & Prescher, J. A. Developing bioorthogonal probes to span a spectrum of
1112 reactivities. *Nat Rev Chem* **4**, 476–489 (2020).
1113 69. Sakuragi, T. & Nagata, S. Regulation of phospholipid distribution in the lipid bilayer by
1114 flippases and scramblases. *Nat. Rev. Mol. Cell Biol.* **24**, 576–596 (2023).
1115 70. Surma, M. A., Klose, C. & Simons, K. Lipid-dependent protein sorting at the trans-Golgi
1116 network. *Biochim. Biophys. Acta* **1821**, 1059–1067 (2012).
1117 71. Sharpe, H. J., Stevens, T. J. & Munro, S. A comprehensive comparison of transmembrane
1118 domains reveals organelle-specific properties. *Cell* **142**, 158–169 (2010).
1119 72. Carpenter, M. A. *et al.* Protein Proximity Observed Using Fluorogen Activating Protein and
1120 Dye Activated by Proximal Anchoring (FAP-DAPA) System. *ACS Chem. Biol.* **15**,
1121 2433–2443 (2020).
1122 73. Telmer, C. A. *et al.* Rapid, specific, no-wash, far-red fluorogen activation in subcellular
1123 compartments by targeted fluorogen activating proteins. *ACS Chem. Biol.* **10**, 1239–1246
1124 (2015).
1125 74. Kowarz, E., Löscher, D. & Marschalek, R. Optimized Sleeping Beauty transposons rapidly
1126 generate stable transgenic cell lines. *Biotechnol. J.* **10**, 647–653 (2015).
1127 75. Jao, C. Y., Roth, M., Welti, R. & Salic, A. Biosynthetic labeling and two-color imaging of
1128 phospholipids in cells. *Chembiochem* **16**, 472–476 (2015).
1129 76. Sparkes, B. L., Slone, E. E. A., Roth, M., Welti, R. & Fleming, S. D. Intestinal lipid

alterations occur prior to antibody-induced prostaglandin E2 production in a mouse model of ischemia/reperfusion. *Biochim. Biophys. Acta* **1801**, 517–525 (2010).

77. Zhou, Z. *et al.* LipidomeDB data calculation environment: online processing of direct-infusion mass spectral data for lipid profiles. *Lipids* **46**, 879–884 (2011).

78. Montagut, A. M., Gálvez, E., Shafir, A., Sebastián, R. M. & Vallribera, A. Triarylmethane Dyes for Artificial Repellent Cotton Fibers. *Chemistry* **23**, 3810–3814 (2017).

79. Kim, J., Park, E. Y., Moon, S.-Y., Kim, J.-M. & Park, K. Patterned color images with a triphenylmethane-derived acrylate polymer. *Macromol. Res.* **16**, 81–83 (2008).